

Lifshitz transitions in RCo_5 ($\text{R}=\text{Y}, \text{La}$) and in Osmium

DISSERTATION

zur Erlangung des akademischen Grades

Doctor rerum naturalium
(Dr. rer. nat.)

vorgelegt

der Fakultät Mathematik und Naturwissenschaften
der Technischen Universität Dresden

von

DANIELA KOUDELA

geboren am 18. Dezember 1975 in Frankenthal/Pfalz

LEIBNIZ-INSTITUT FÜR FESTKÖRPER- UND
WERKSTOFFFORSCHUNG DRESDEN

Gutachter: Prof. Dr. Helmut Eschrig

Prof. Dr. Niels E. Christensen

Prof. Dr. Yuri Grin

Eingereicht am: 17.8.2006

Tag der Verteidigung: 20.2.2007

CONTENTS

List of abbreviations	5
1 Introduction	7
2 Theory	11
2.1 DFT for the ground state	11
2.1.1 Non-relativistic Density Functional Theory	12
2.1.2 Relativistic Density Functional Theory	14
2.2 Magneto-elastic effects	16
2.2.1 Hydrostatic pressure	16
2.2.2 Bulk modulus	18
2.2.3 Magnetism under pressure	18
2.3 Lifshitz transitions	21
2.3.1 From band structure to Fermi surfaces	22
2.3.2 The density of states	23
2.3.3 Topological changes of the Fermi surface	24
2.3.4 Anomalies of thermodynamic and other quantities in- duced by an ETT	31
3 Results	33
3.1 Isomorphic volume collapse of YCo_5 under pressure	33
3.1.1 Structure of YCo_5	34

3.1.2	Method of calculation	35
3.1.3	Convergence of parameters	36
3.1.4	Fixed Spin Moment calculations	37
3.1.5	The magnetic moment of YCo_5 under pressure	39
3.1.6	Lattice geometry and elastic anomaly under pressure	41
3.1.7	Behavior of lattice constants under pressure	45
3.1.8	Transition to non-magnetic state	46
3.1.9	Band structure and DOS of YCo_5	47
3.1.10	The Fermi surface of YCo_5	47
3.1.11	Conclusions	51
3.2	Predictions for LaCo_5 under pressure	54
3.2.1	Method of calculation	54
3.2.2	Convergence of parameters	55
3.2.3	The magnetic moment of LaCo_5 under pressure	56
3.2.4	Lattice geometry and elastic anomaly under pressure	58
3.2.5	Band structure and DOS of LaCo_5	60
3.2.6	Conclusions	62
3.3	Lifshitz transitions in Os under pressure	62
3.3.1	Method of calculation	64
3.3.2	Total energy calculations	64
3.3.3	The Fermi surface of Osmium under pressure	64
3.3.4	Band structure of Osmium under pressure	69
3.3.5	DOS of Osmium	70
3.3.6	Lattice geometry under pressure	73
3.3.7	A good fit to $(c/a)(P)$	76
3.3.8	Conclusions	78
3.3.9	Values of adjustable parameters used in Table 3.2	78
4	Summary	81
	Bibliography	88

LIST OF ABBREVIATIONS

ASA	Atomic Sphere Approximation
BZ	Brillouin Zone
DFT	Density Functional Theory
DOS	Density Of States
ETT	Electronic Topological Transition
FPLO	Full-Potential nonorthogonal Local-Orbital minimum-basis band-structure scheme
FSM	Fixed Spin Moment
HS	High Spin
LDA	Local Density Approximation
LMTO	Linear Muffin-Tin Orbital
LS	Low Spin
LSDA	Local Spin Density Approximation
RDFT	Relativistic Density Functional Theory
SDFT	Spin Density Functional Theory

Chapter 1

INTRODUCTION

For designing new materials with given properties needed for technical applications it is important to understand the connection between electronic structure and observable qualities like elastic properties or magnetism.

An important tool for this task is Density Functional Theory (DFT), which is based on the two articles of Hohenberg and Kohn [1] and Kohn and Sham [2] and was later set to a solid mathematical basis by Lieb [3]. With the help of DFT one can reduce the complicated many-body problem, which one faces when trying to describe a solid, to an effective one-particle problem and this way making the ab-initio calculation of solids feasible. DFT yields the total energy and the so-called band structure from which the Fermi surface can be calculated. Furthermore, DFT can be generalized to a spin polarized case (Spin Density Functional Theory, SDFT), where it is possible to calculate magnetic moments.

The equations one has to solve when applying (S)DFT to a material are implemented in computer codes like FPLO (Full-Potential nonorthogonal Local-Orbital minimum-basis band-structure scheme, [4]), the program which was used for the calculation of the results presented in this thesis.

In my thesis I concentrated on anomalies induced by topological changes

of the Fermi surface, which are called "Lifshitz transitions" [5, 6]. Lifshitz transitions are an interesting subject to study because a topological transition of the Fermi surface results in a van Hove singularity in the density of states (DOS) at the Fermi energy, which again induces an anomaly in the free energy and therefore yield anomalies of observable physical quantities.

To investigate Lifshitz transitions in magnetic and non-magnetic materials, RCo_5 ($\text{R}=\text{Y}, \text{La}$) was chosen as an example for a magnetic system and Osmium was chosen to explore a non-magnetic example.

YCo_5 is a very interesting compound to study because it is the parent compound of SmCo_5 , an important magnetic compound for technical applications. To understand the magnetism in SmCo_5 it is necessary to know, which magnetic contributions come from the Samarium atoms and which from the Cobalt atoms. The magnetic contribution arising from Co can be studied by exploring YCo_5 since Yttrium has no f -electrons, which are responsible for the magnetism in Samarium.

The calculations show, that in YCo_5 a transition from strong ferromagnetism to weak ferromagnetism takes place, where the magnetic moment switches from a high moment state to a low moment state under pressure. This drop of the magnetic moment causes a volume collapse and is accompanied by an opposed shift of spin-up and spin-down bands, which result into totally different Fermi surfaces for the high moment and the low moment state. Because the electronic configuration in LaCo_5 is very similar to the one in YCo_5 , we expect a similar transition in LaCo_5 on the basis of our calculations. For YCo_5 our predictions have been confirmed by experiment [7], where a volume collapse was found under pressure. For LaCo_5 there are no experiments done so far to the best of our knowledge.

In the case of Os there are contradictory experiments [8, 9]. Occelli *et al.* [8] measured Os under pressure and found an anomaly in the c/a ratio under applied pressure. They claimed that this could be an evidence for a Lifshitz transition. Takemura [9] did measurements in the same pressure range. He did not find any anomaly in his data. So we decided to calculate the behavior of Os under pressure to find out, what theory yields. Our calculations show three Lifshitz transitions, but at much higher pressures than applied in the experiments. Furthermore, the resulting anomalies in the DOS are much too small to have the chance of being observed experimentally.

The goal of this study is to examine, if YCo_5 and LaCo_5 show elastic anomalies under pressure. The aim for Os is to find Lifshitz transitions under pressure and to explore if they result in anomalies of the c/a ratio

versus pressure.

The thesis is structured like follows:

- Chapter 2 sets the theoretical basics needed for calculation and discussion of the results. These basics are a short introduction into DFT for the ground state, magneto-elastic effects and a section about Lifshitz transitions.
- Then the results of the calculations about YCo_5 , LaCo_5 and Osmium are presented and discussed in Chapter 3.
- Finally Chapter 4 summarizes the most important results.

Chapter 2

THEORY

In this chapter the theoretical basics needed for calculation and discussion of the results shown in Chapter 3 are presented. The first part of this chapter contains a short introduction into DFT on which FPLO [4] – the code with which the results are calculated – is based. The next part deals with magneto-elastic effects, which are important in my work on YCo_5 and LaCo_5 . The last and largest part of this chapter is about Lifshitz transitions, which take place in YCo_5 , LaCo_5 and in Osmium.

2.1 DFT FOR THE GROUND STATE

This section gives an overview over the principles of DFT. Here the original approach is presented, which lacks mathematical rigor but is straight forward in a sense that all quantities and approximations, which are needed for the calculation are introduced at that moment they are needed. Another way of presenting DFT is by applying convex functional analysis. This was done in the early eighties by Lieb [3] and put DFT on solid mathematical basis. At the end of this chapter a few remarks on Relativistic Density Functional Theory (RDFT) are given.

2.1.1 Non-relativistic Density Functional Theory

To calculate the total energy of the ground state of some bulk material, the first ansatz would be the solution of the eigenvalue equation of the Hamiltonian

$$E = \min_{\Psi} \langle \Psi | H | \Psi \rangle \quad (2.1)$$

with

$$\hat{H} = -\frac{1}{2} \sum_{i=1}^N \Delta_i - \sum_{i=1}^N \sum_{j=1}^M \frac{Z_j}{|\mathbf{r}_i - \mathbf{R}_j|} + \frac{1}{2} \sum_{i \neq j}^N \frac{1}{|\mathbf{r}_i - \mathbf{r}_j|} + \frac{1}{2} \sum_{i \neq j}^M \frac{Z_i Z_j}{|\mathbf{R}_i - \mathbf{R}_j|}. \quad (2.2)$$

Here the first term is the kinetic energy of the electrons, the second gives the Coulomb-interaction between electrons and ion cores, the third represents the Coulomb-interaction between the electrons and the last gives the Coulomb-interaction between the ion cores.

But to solve Eq. (2.1) with the Hamiltonian (2.2) is a very hopeless venture, since the many-particle wave function of a solid has of the order of 10^{23} variables even if one applies the adiabatic approximation to decouple the ion cores from the valence electrons and treat the former as an external potential.

In 1927 Thomas and Fermi developed an explicit but naïve theory in which the total energy was calculated as a functional of both the density of the electrons and the external potential coming from the ion cores. They approximated the kinetic energy of the electrons (first term in Eq. (2.2)) in the solid with the kinetic energy of the homogeneous interaction-free fermion gas, which can be seen as a crude approximation to DFT.

In 1964 Hohenberg and Kohn proved "that there exists a universal functional of the density, $F[n(\mathbf{r})]$, independent of $V(\mathbf{r})$, such that the expression

$$E = \int d^3r V(\mathbf{r})n(\mathbf{r}) + F[n(\mathbf{r})] \quad (2.3)$$

has as its minimum value the correct ground-state energy associated with $V(\mathbf{r})$ " [1] under the constraint

$$N[n] = \int d^3r n(\mathbf{r}) = N \quad (2.4)$$

of particle conservation. Their theorem on which DFT is based, states that *"the potential $V(\mathbf{r})$ is modulo a constant a unique function of the density*

$n(\mathbf{r})$ ” [1]. Unfortunately the functional $F[n]$ is not known and most probably it will never be known. To be able to do calculations anyway Kohn and Sham [2] proposed the following decomposition of $F[n]$:

$$F[n] = T_s[n] + U[n] + E_{xc}[n]. \quad (2.5)$$

Here,

$$T_s[n] = \min_{\phi_i} \left\{ \sum_{i=1}^N \int d^3r \phi_i^*(\mathbf{r}) \left(-\frac{\Delta}{2} \right) \phi_i(\mathbf{r}) \middle| n(\mathbf{r}) = \sum_{i=1}^N |\phi_i(\mathbf{r})|^2, \langle \phi_i | \phi_j \rangle = \delta_{ij} \right\} \quad (2.6)$$

is the kinetic energy of the ground state of a system of noninteracting electrons with density $n(\mathbf{r})$.

$$U[n] = \frac{1}{2} \int d^3r \int d^3r' \frac{n(\mathbf{r})n(\mathbf{r}')}{|\mathbf{r} - \mathbf{r}'|} \quad (2.7)$$

gives the Hartree-energy. The last term, the exchange-correlation energy $E_{xc}[n]$ includes all contributions to the total energy, which are missed in the other terms.

For the calculation of $E_{xc}[n]$ they proposed the model which is now known as *Local Density Approximation* (LDA) and substitutes the exchange-correlation energy with the exchange-correlation energy of a uniform electron gas of density $n(\mathbf{r})$:

$$E_{xc}[n] = \int d^3r n(\mathbf{r}) \epsilon_{xc}(n(\mathbf{r})) \quad (2.8)$$

where $\epsilon_{xc}(n(\mathbf{r}))$ is the exchange-correlation energy per electron of a uniform electron gas of density n . This quantity can be calculated and gives a good approximation if the density $n(\mathbf{r})$ is slowly varying.

If one varies Eq. (2.3) under the constraint of Eq. (2.4) with respect to the particle density $n(\mathbf{r})$:

$$\frac{\delta}{\delta n(\mathbf{r}')} \left(\int d^3r V(\mathbf{r})n(\mathbf{r}) + F[n(\mathbf{r})] - \mu \int d^3r n(\mathbf{r}) \right) = 0 \quad (2.9)$$

one gets

$$V(\mathbf{r}') + \frac{\delta T_s[n]}{\delta n(\mathbf{r}')} + \frac{\delta U[n]}{\delta n(\mathbf{r}')} + \frac{\delta E_{xc}[n]}{\delta n(\mathbf{r}')} - \mu = 0. \quad (2.10)$$

If one compares Eq. (2.10) with the analogous equation of a system of non-interacting electrons, which reads

$$V(\mathbf{r}') + \frac{\delta T_s[n]}{\delta n(\mathbf{r}')} - \mu = 0 \quad (2.11)$$

one can reduce the many-body equation to an effective one-particle equation by the substitution

$$V(\mathbf{r}') + \frac{\delta U[n]}{\delta n(\mathbf{r}')} + \frac{\delta E_{xc}[n]}{\delta n(\mathbf{r}')} = V_{eff}(\mathbf{r}'). \quad (2.12)$$

Variation of Eq. (2.3) with respect to $\phi_j^*(\mathbf{r}')$ leads to the Kohn-Sham equations

$$\left[-\frac{\Delta}{2} + V_{eff}(\mathbf{r}') \right] \phi_j(\mathbf{r}') = \phi_j(\mathbf{r}') \varepsilon_j \quad (2.13)$$

which have the same form than the one-particle Schrödinger equation.

The way to solve Eq. (2.13) is a self-consistent one: At first one guesses a density $n_{in}(\mathbf{r})$ and calculates the effective potential (2.12). Then one solves the Kohn-Sham equations (2.13), which yield ε_j and $\phi_j(\mathbf{r})$. From the $\phi_j(\mathbf{r})$ one can calculate a new density $n_{out}(\mathbf{r})$. If

$$\frac{1}{V} \int_V d^3r |n_{out}(\mathbf{r}) - n_{in}(\mathbf{r})| \leq tol \quad (2.14)$$

where tol is a small number determining the accuracy of the density, the problem is solved. If not, one has to start a new iteration. The input-density of the next iteration is usually a linear combination of the output-density (densities) and the input-density of the last (few) iteration(s).

2.1.2 Relativistic Density Functional Theory

In heavy atoms relativistic effects become important. The reason is that in atomic units the average velocity of an electron in an atom is proportional to Z and $c = 137$, where Z is the nuclear charge and c is the velocity of light.

To formulate a relativistic version of DFT one substitutes the density n by the four-current-density J^μ , the potential V by the four-potential A_μ and the Hamiltonian by a Hamiltonian including not only the rest mass in the kinetic energy but taking as well relativistic many-body effects like the Breit-interaction into account. One can then derive the relativistic DFT in analogy to the non-relativistic case (for details see [10, 11]) and arrive at the Kohn-Sham-Dirac equation

$$\left(-ic\boldsymbol{\alpha} \cdot \boldsymbol{\nabla} + \beta c^2 - ec\beta\gamma^\mu (A_\mu + \delta_\mu^0 A_0^H + A_\mu^{xc}) \right) \psi_i = \psi_i \varepsilon_i \quad (2.15)$$

with

$$J^\mu = c \sum_{i=1}^N n_i \psi_i^\dagger \gamma^0 \gamma^\mu \psi_i, \quad (2.16)$$

$$\langle \psi_i^\dagger | \psi_j \rangle = \delta_{ij}, \quad (2.17)$$

e being the electrodynamic charge quantum and $0 \leq n_i \leq 1$ are orbital occupation numbers of the Dirac spinor orbitals $\psi_i(\mathbf{r})$. Here,

$$\boldsymbol{\alpha} = \begin{pmatrix} 0 & \boldsymbol{\sigma} \\ \boldsymbol{\sigma} & 0 \end{pmatrix}, \beta = \gamma^0 = \begin{pmatrix} \mathbb{1} & 0 \\ 0 & -\mathbb{1} \end{pmatrix}, \boldsymbol{\gamma} = \begin{pmatrix} 0 & \boldsymbol{\sigma} \\ -\boldsymbol{\sigma} & 0 \end{pmatrix}. \quad (2.18)$$

A_0^H and A_μ^{xc} are the relativistic equivalents of the Hartree potential and the exchange-correlation potential.

The total energy E in the relativistic case is calculated as

$$E = T[n] + E_{xc}[n] + U[n] + \int d^3r V(\mathbf{r})n(\mathbf{r}) + E_{nucl} \quad (2.19)$$

where $E_{xc}[n]$ and $U[n]$ are the same than in the non-relativistic case (Eq.s 2.7 and 2.8) and the kinetic energy $T[n]$ as well as the Coulomb energy of the nuclei E_{nucl} are calculated like

$$T[n] = \sum_{i=1}^N \varepsilon_i - \int d^3r V_{eff}(\mathbf{r})n(\mathbf{r}) - \sum_{i=1}^N \langle \psi_i | \beta \Sigma_z B^{cr} | \psi_i \rangle \quad (2.20)$$

$$E_{nucl} = \frac{1}{2} \sum_{i \neq j}^M \frac{Z_i Z_j}{|\mathbf{R}_i - \mathbf{R}_j|}. \quad (2.21)$$

Here, B^{cr} is the exchange-correlation field and Σ_z is the z -component of

$$\boldsymbol{\Sigma} = \begin{pmatrix} \boldsymbol{\sigma} & 0 \\ 0 & \boldsymbol{\sigma} \end{pmatrix}. \quad (2.22)$$

It should be noted that one has to face many problems when deriving a relativistic version of DFT but to deal with them is not the aim of this thesis. The interested reader is referred to [10, 12].

While this full-relativistic version of DFT was used to calculate the results presented in Section 3.3, in Section 3.1 and Section 3.2 the calculations were done in a *scalar relativistic* way. Doing a calculation not fully relativistic but scalar relativistic has the advantage, that the rank of the eigenvalue problem is reduced by a factor of two due to the decoupling of spin-up and spin-down states [13]. The price one has to pay for this is, that in scalar relativistic schemes spin-orbit coupling is neglected.

2.2 MAGNETO-ELASTIC EFFECTS

In this section only those magneto-elastic effects should be described, which are related to my work on YCo_5 , which is the connection between hydrostatic pressure and lattice geometry, the definition of the bulk modulus and the effect of pressure on magnetization. For all other magneto-elastic effects the interested reader is referred to [14].

2.2.1 Hydrostatic pressure

One can deform a material by applying pressure. There are different ways pressure can be exerted to a material because stress in general is a tensor quantity. Pressure can be applied in only one direction (uniaxial pressure) or it can be applied in more than one directions. If the absolute value of the pressure is the same in all directions, that is the stress tensor is $\sigma = -P\mathbb{1}$, the pressure is called *hydrostatic*.

Hydrostatic pressure is a thermodynamic quantity, which can be calculated if the dependence of the total energy on volume is known:

$$P = -\frac{dE}{dV}. \quad (2.23)$$

In electronic structure calculations the total energy E in dependence of the lattice geometry (lattice constants, angles and internal parameters) is calculated. If the unit cell is cubic ($a = b = c$ and $V = a^3$)

$$P = -\frac{dE}{da} \frac{da}{dV} = -\frac{1}{3a^2} \frac{dE}{da}. \quad (2.24)$$

But how does a hexagonal unit cell deform under hydrostatic pressure? Will the c/a ratio stay constant or is another c/a ratio lower in energy if pressure is exerted on the material? The unit cell volume of the hexagonal lattice depends on the lattice constants like

$$V = \frac{\sqrt{3}}{2} a^2 c. \quad (2.25)$$

Pressure is force per area and so we have for the pressure along the c -direction

$$P_c = -\frac{\partial E}{\partial c} \bigg|_a \frac{\partial c}{\partial V} \bigg|_a = -\frac{\partial E}{\partial c} \bigg|_a \cdot \frac{2}{\sqrt{3}a^2}. \quad (2.26)$$

The pressure along the a -direction is

$$P_a = -\frac{\partial E}{\partial a} \bigg|_c \frac{\partial a}{\partial V} \bigg|_c = -\frac{\partial E}{\partial a} \bigg|_c \cdot \frac{1}{\sqrt{3}ac}. \quad (2.27)$$

Both pressures must be the same in the hydrostatic case. Setting

$$P_c = P_a \quad (2.28)$$

leads to

$$2\frac{c}{a} \frac{\partial E}{\partial c} \bigg|_a = \frac{\partial E}{\partial a} \bigg|_c. \quad (2.29)$$

Now we have to transform the derivatives with respect to a and c to derivatives with respect to V and c/a :

$$\frac{dE}{da} = \frac{\partial E}{\partial V} \frac{dV}{da} + \frac{\partial E}{\partial(c/a)} \frac{d(c/a)}{da} \quad (2.30)$$

$$\frac{dE}{dc} = \frac{\partial E}{\partial V} \frac{dV}{dc} + \frac{\partial E}{\partial(c/a)} \frac{d(c/a)}{dc} \quad (2.31)$$

with

$$\begin{pmatrix} \frac{\partial V}{\partial a} & \frac{\partial V}{\partial c} \\ \frac{\partial(c/a)}{\partial a} & \frac{\partial(c/a)}{\partial c} \end{pmatrix} = \begin{pmatrix} \sqrt{3}ac & \sqrt{3}a^2/2 \\ -c/a^2 & 1/a \end{pmatrix}. \quad (2.32)$$

Substituting Eq.s (2.30) and (2.31) into Eq. (2.29) yields

$$2\frac{c}{a} \left(\frac{\sqrt{3}a^2}{2} \frac{\partial E}{\partial V} + \frac{1}{a} \frac{\partial E}{\partial(c/a)} \right) = \sqrt{3}ac \frac{\partial E}{\partial V} - \frac{c}{a^2} \frac{\partial E}{\partial(c/a)}, \quad (2.33)$$

which can be simplified to the hydrostatic pressure condition

$$\frac{\partial E}{\partial(c/a)} \bigg|_{V_0} = 0. \quad (2.34)$$

This means that under hydrostatic pressure the c/a ratio will have that value where the energy is minimum for the given volume. With the help of Eq. (2.34) we can assign to every volume a c/a ratio.

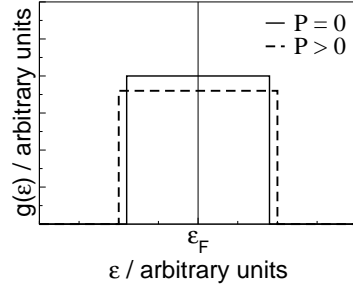


Figure 2.1: DOS for one band crossing the Fermi level. For simplicity the DOS is taken to be constant over the whole band. If the band broadens under pressure, the DOS has to decrease to keep the number of electrons constant.

2.2.2 Bulk modulus

If we calculate the second derivative of the total energy with respect to volume (and having at each volume the c/a ratio relaxed) we arrive at a quantity, which is proportional to the bulk modulus B_0 . The definition of the bulk modulus is

$$B_0 = V_0 \left. \frac{\partial^2 E}{\partial V^2} \right|_{V_0}. \quad (2.35)$$

The bulk modulus is a measure for the force needed to compress the sample. The reciprocal of it is called *compressibility*. The harder it is to compress a sample the bigger is its bulk modulus and the smaller is its compressibility. The value of the bulk modulus changes under pressure. Usually one expects the bulk modulus to grow under increasing pressure.

2.2.3 Magnetism under pressure

If pressure is applied to a sample, the volume of the unit cell shrinks and the atoms move closer together. If the distance between the atoms is decreasing, the overlap of their orbitals will increase and the bands broaden. If the bands get broader, the DOS $g(\varepsilon)$ (for the definition of the DOS see Chapter 2.3.2) must get smaller on average because the total number of electrons N stays the same. This is illustrated in Fig. 2.1. But what consequences concerning magnetism does a smaller DOS have?

To derive the link to magnetism we will make an excursion to Stoner theory (see Chapter 4.1.1 of [15]). Consider the total energy E of the electrons.

If the derivative of the total energy with respect to the magnetization M equals zero for some magnetization M_0 , there is an extremum in the total energy. This extremum will be a stable state if the second derivative of the total energy with respect to magnetization is greater than zero (minimum of energy) or an unstable state if it is smaller than zero (maximum of energy). If there is a maximum for $M_0 = 0$ in the total energy E , the non-magnetic state will be unstable and the sample has a magnetic moment greater than zero.

To derive an inequality (the famous *Stoner criterion*), which provides an idea, if a substance may show magnetism, we will approximate the DOS for each spin-direction (+ or -) by the free electron expression

$$g_{\pm}(\varepsilon) = \frac{3}{4}N \frac{\sqrt{\varepsilon}}{\varepsilon_F^{3/2}} \quad (2.36)$$

with ε_F being the Fermi energy and N being the total number of electrons. We denote with n_+ the total number of electrons with spin-up and with n_- the total number of electrons with spin-down, so that we have

$$N = n_+ + n_-, \quad (2.37)$$

where n_+ and n_- can be calculated from the DOS like

$$n_{\pm} = \int_0^{\varepsilon_{F\pm}} d\varepsilon g_{\pm}(\varepsilon). \quad (2.38)$$

Here, ε_{F+} and ε_{F-} denote spin-up and spin-down band Fermi energies, which are defined to be the distance from the respective band bottom $\varepsilon_{b\pm}$ to the common Fermi energy

$$\varepsilon_{F\pm} = \varepsilon_F - \varepsilon_{b\pm} \quad (2.39)$$

(see Fig. 2.2). The magnetization M of the sample is the difference between spin-up and spin-down electrons

$$M = n_+ - n_-. \quad (2.40)$$

Thus, we can write

$$\frac{\varepsilon_{F\pm}}{\varepsilon_F} = \left(\frac{N \pm M}{N} \right)^{2/3}. \quad (2.41)$$

Due to the magnetization of the sample, the electrons feel a molecular field H_m , which is proportional to the magnetization

$$H_m = -IM. \quad (2.42)$$

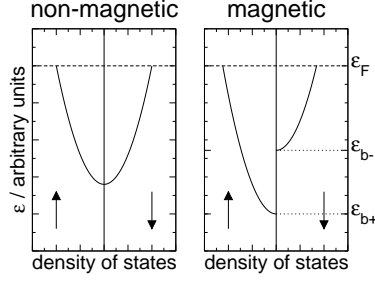


Figure 2.2: DOS for the non-magnetic and for the magnetic case. In the magnetic case, the DOS for the spin-up states is shifted in that way, that it is energetically more favorable for the electrons to occupy spin-up states and the DOS for the spin-down states is shifted in the other direction, so that the total number of electrons stays constant.

The total energy E of the electrons in this approximation can be calculated as

$$\begin{aligned} E &= \int_0^{\varepsilon_F^+} d\varepsilon \varepsilon g_+(\varepsilon) + \int_0^{\varepsilon_F^-} d\varepsilon \varepsilon g_-(\varepsilon) - \frac{1}{2}IM^2 \\ &= \frac{3}{10}N\varepsilon_F \left(\left(1 + \frac{M}{N}\right)^{5/3} + \left(1 - \frac{M}{N}\right)^{5/3} \right) - \frac{1}{2}IM^2. \end{aligned} \quad (2.43)$$

Now we differentiate Eq. (2.43) with respect to the magnetization and do the same with the resulting derivative

$$\frac{dE}{dM} = \frac{\varepsilon_F}{2} \left(\left(1 + \frac{M}{N}\right)^{2/3} - \left(1 - \frac{M}{N}\right)^{2/3} \right) - IM, \quad (2.44)$$

$$\frac{d^2E}{dM^2} = \frac{\varepsilon_F}{3N} \left(\left(1 + \frac{M}{N}\right)^{-1/3} + \left(1 - \frac{M}{N}\right)^{-1/3} \right) - I. \quad (2.45)$$

It is obvious that Eq. (2.44) is zero for $M = 0$. This means that the total energy has an extremum at the non-magnetic state. For $M = 0$ Eq. (2.45) yields

$$\frac{d^2E}{dM^2} = \frac{2\varepsilon_F}{3N} - I = \frac{1}{g(\varepsilon_F)} - I \quad (2.46)$$

with

$$g(\varepsilon) = g_+(\varepsilon) + g_-(\varepsilon). \quad (2.47)$$

This means that magnetism is favored if

$$1 < g(\varepsilon_F)I. \quad (2.48)$$

Eq. (2.48) is the famous Stoner criterion.

How does the Stoner criterion help us to draw any conclusions about magnetism under pressure? Before this excursion on Stoner theory we stated that when the bands broaden under pressure the DOS should decrease because of the constant electron number. In particular the DOS at the Fermi level should decrease, which decreases the Stoner product $g(\varepsilon_F)I$. If its value falls below 1, the non-magnetic state is either stable or at least meta-stable.

So we conclude, that under a certain pressure the material under consideration should loose its spontaneous magnetization. If the DOS has structure in the energy range of the exchange splitting, the situation is a bit more involved, and partial effects are possible.

2.3 LIFSHITZ TRANSITIONS

For understanding or even predicting the properties and peculiarities of a metal, the knowledge of band structure and Fermi surface is important. Changing external parameters (e. g. pressure) may induce changes in the band structure and the Fermi surface.

In 1960 I. M. Lifshitz predicted a special "electron transition" [5], which takes place when the topology of the Fermi surface changes. Such changes can be induced by alloying or applying pressure to the material. The consequences of a topological change of the Fermi surface are anomalies of the DOS near the Fermi energy and anomalies of the electron dynamics. These lead to anomalies of thermodynamic and kinetic electron characteristics of the metal, which result in anomalies of observable physical quantities. Nevertheless these anomalies in some cases may be too small to be observed experimentally. Another difficulty for experimental detection of those topological changes is, that temperature or impurities will smear out the effect.

The publication of Lifshitz's paper caused a huge amount of theoretical and experimental work (see [6, 16, 17] and references therein) to find Lifshitz transitions in different materials and investigate the corresponding anomalies.

In this section, at first, the connection between band structure and Fermi surface will be established. Then some general formulas for calculating the DOS will be derived. After that, topological changes of the Fermi surface

will be considered in detail and the DOS around these electronic topological transitions will be calculated. The section finishes with the calculation of the thermodynamic potential around the transition.

2.3.1 From band structure to Fermi surfaces

In an atom there are several discrete energy levels. If two atoms form a molecule those energy levels will split into a bonding and an anti-bonding level. In a solid with about 10^{23} atoms the discrete energy levels will broaden into bands with energy $\varepsilon(\mathbf{k})$, where \mathbf{k} denotes the crystal momentum. The gradient of an energy band $\varepsilon_n(\mathbf{k})$ with respect to \mathbf{k} is proportional to the velocity of the corresponding electron

$$\mathbf{v}_n(\mathbf{k}) = \frac{1}{\hbar} \nabla_{\mathbf{k}} \varepsilon_n(\mathbf{k}) = \frac{1}{\hbar} \frac{\partial \varepsilon_n(\mathbf{k})}{\partial \mathbf{k}}. \quad (2.49)$$

Since the crystal is periodic, each band $\varepsilon_n(\mathbf{k})$ has at least one minimum and one maximum within the Brillouin zone (BZ). At these points the velocity of the electron is zero (compare Eq. (2.49)). Points at which the electronic velocity is zero, are called *van Hove singularities*. The term "singularity" is due to the fact that the reciprocal value of the electronic velocity is needed for calculating the electronic DOS (see Eq. (2.56)).

At $T = 0$ all states with energies $\varepsilon_n(\mathbf{k}) \leq \varepsilon_F$ will be occupied and all states with energies $\varepsilon_n(\mathbf{k}) \geq \varepsilon_F$ will be unoccupied. This defines the Fermi energy ε_F . At temperatures $T > 0$ the occupation of the states changes. The probability of a state being occupied at a certain temperature T is given by the Fermi function

$$f(\varepsilon, \mu, T) = \frac{1}{\exp\left(\frac{\varepsilon - \mu}{k_B T}\right) + 1}. \quad (2.50)$$

Let us focus on the case $T = 0$ and solve the equation

$$\varepsilon_n(\mathbf{k}) = \varepsilon_F. \quad (2.51)$$

This equation has only solutions if the solid is a metal (compare Fig. 2.3). The set of points in \mathbf{k} -space which fulfill Eq. (2.51) is called *Fermi surface*.

One of the easiest cases of a Fermi surface is the Fermi surface of free electrons. It has the shape of a sphere since their band structure is given by $\varepsilon(\mathbf{k}) = \hbar^2 k^2 / (2m)$. In general the Fermi surface can consist of many disconnected pockets with a broad variety in shape. One distinguishes between two kinds of Fermi surfaces:

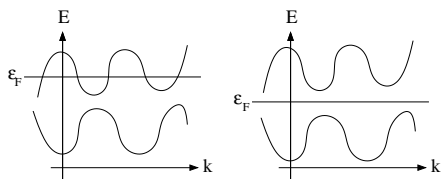


Figure 2.3: The left picture shows the schematic band structure of a metal and the right one shows the schematic band structure of an insulator. Both are distinguished only by the location of the Fermi energy: in a metal the Fermi energy is lying in a band inducing a partial occupation of this band and in an insulator the Fermi level lies in a band gap.

- hole surfaces and
- electron surfaces.

Hole surfaces contain unoccupied states and therefore correspond to maxima in the band structure, electron surfaces correspond to minima in the band structure because they contain occupied states. The electron velocity vectors are pointing inward if the Fermi surface is an hole surface and they are pointing outward if the Fermi surface is an electron surface.

Another property of Fermi surfaces is, that they can be open or closed. Closed surfaces fit into one BZ and open surfaces extend to opposite zone boundaries.

2.3.2 The density of states

An important quantity when dealing with materials properties determined by electronic structure is the DOS $g(\varepsilon)$ [18]. The DOS is connected to the total number of electrons per unit cell by

$$N(\varepsilon_F) = \int_{-\infty}^{\varepsilon_F} d\varepsilon g(\varepsilon) = N. \quad (2.52)$$

Another way to calculate the total number of electrons is calculating the volume of the Fermi surface and multiplying it with the number of allowed \mathbf{k} -values per unit volume of \mathbf{k} -space

$$N(\varepsilon_F) = 2 \cdot \frac{V}{8\pi^3} \cdot \int_{\varepsilon \leq \varepsilon_F} d^3k = 2 \cdot \frac{V}{8\pi^3} \cdot \sum_n \int d^3k \theta(\varepsilon_F - \varepsilon_n(\mathbf{k})). \quad (2.53)$$

The factor 2 is due to spin degeneracy. If there is no spin degeneracy, Eq. (2.53) reads

$$N(\varepsilon_F) = \frac{V}{8\pi^3} \cdot \sum_{n\sigma} \int d^3k \theta(\varepsilon_F - \varepsilon_{n\sigma}(\mathbf{k})). \quad (2.54)$$

From Eq. (2.52) we can calculate the DOS

$$g(\varepsilon) = \frac{dN}{d\varepsilon} = \frac{V}{8\pi^3} \cdot \sum_{n\sigma} \int d^3k \delta(\varepsilon - \varepsilon_{n\sigma}(\mathbf{k})) \quad (2.55)$$

$$= \frac{V}{8\pi^3} \cdot \sum_{n\sigma} \int_\varepsilon dS \frac{1}{\left| \frac{\partial \varepsilon_{n\sigma}(\mathbf{k})}{\partial \mathbf{k}} \right|}. \quad (2.56)$$

Here dS denotes an infinitesimal area of the Fermi surface.

To proceed from Eq. (2.55) to Eq. (2.56) one can use

$$\delta(f(x)) = \sum_i \frac{1}{\left| \frac{df}{dx} \right|_{x=x_i}} \delta(x - x_i), \quad (2.57)$$

where i denotes all single zeros of the function $f(x)$. Eq. (2.57) is not valid for multiple zeros. The integral of Eq. (2.55) is removed by the δ -function of Eq. (2.57). The surface integral of Eq. (2.56) arises from the sum over all zeros in Eq. (2.57).

2.3.3 Topological changes of the Fermi surface

One can vary the Fermi surface by varying the Fermi energy and/or the band structure. Possible methods for changing the band structure and the relative position of the Fermi energy within the band structure are for example alloying or the application of pressure. If either variation yields a topological change of the Fermi surface, one calls it a "*Lifshitz transition*", "*electronic topological transition*" (ETT), or " *$2\frac{1}{2}$ order phase transition*", which takes place, if a van Hove singularity (at ε_{cr}) passes the Fermi level: $\varepsilon_F = \varepsilon_{cr}$.

The name "Lifshitz transition" arises from a publication by I. M. Lifshitz [5], where he considers topological changes of the Fermi surface and the resulting consequences for the DOS and other physical properties. The name ETT is clear from its definition and why this transition is sometimes called a " *$2\frac{1}{2}$ order phase transition*" will be explained at the end of Section 2.3.

In three dimensions only four different topological changes of the Fermi surface are possible:

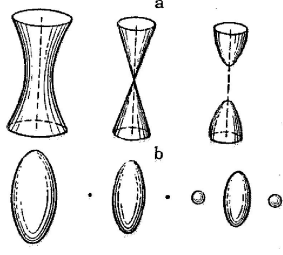


Figure 2.4: Possible topological transitions of the Fermi surface in three dimensions (figure taken from [5]).

- the disruption of a neck in the Fermi surface (see Fig. 2.4a from left to right)
- the creation of a neck in the Fermi surface (see Fig. 2.4a from right to left)
- the creation of a new pocket of the Fermi surface (see Fig. 2.4b from left to right)
- the disappearance of a pocket of the Fermi surface (see Fig. 2.4b from right to left)

Let us now focus at first on the creation or disappearance of a pocket of the Fermi surface and then consider the disruption or creation of a neck.

Ellipsoids in the band structure

Consider the band structure $\varepsilon(\mathbf{k})$ of a solid. Assume at some region for one band $\varepsilon_n(\mathbf{k})$

$$\varepsilon_n(\mathbf{k}) = \varepsilon_{cr} \pm \left(\frac{\hbar^2}{2m_x} (k_x - k_{0x})^2 + \frac{\hbar^2}{2m_y} (k_y - k_{0y})^2 + \frac{\hbar^2}{2m_z} (k_z - k_{0z})^2 \right) \quad (2.58)$$

is a good approximation. The question is now, how does the Fermi surface of such a band look like (if it exists).

The term in the brackets is everywhere greater or equal zero, so that the Fermi energy has to be greater than ε_{cr} in case of the plus sign and smaller than ε_{cr} in case of the minus sign to give additional solutions to Eq. (2.51), that means to give rise to an additional pocket in the Fermi surface.

For simplicity we consider here only the case with the plus sign (electron-surface), the case with the minus sign (hole-surface) is analogous. Another simplification, which does not affect generality, is, that we shift the coordinate-system such, that its origin is at the point \mathbf{k}_0 .

If the Fermi energy is close to ε_{cr} and $\varepsilon_n(\mathbf{k})$ is given by Eq. (2.58), then we can solve Eq. (2.51) for k_z

$$k_z = \pm \sqrt{\frac{2m_z}{\hbar^2} (\varepsilon_F - \varepsilon_{cr}) - \left(\frac{m_z}{m_x} k_x^2 + \frac{m_z}{m_y} k_y^2 \right)}. \quad (2.59)$$

A three-dimensional plot of Eq. (2.59) (Figure 2.5, left panel), shows the pocket of the Fermi surface, which appears when $\varepsilon_F > \varepsilon_{cr}$ and disappears when $\varepsilon_F < \varepsilon_{cr}$. With the minus sign in Eq. (2.58) it would be the other way round. *From the left panel of Figure 2.5 one can conclude that a band structure like in Eq. (2.58) results in an ellipsoid.*

The DOS for such an ellipsoid can be calculated. It is easiest to use Eq. (2.53) for this task and then calculate the derivative with respect to ε . The volume of an ellipsoid is $V_{ellipsoid} = \frac{4}{3}\pi abc$, where a , b and c are determined by

$$1 = \frac{x^2}{a^2} + \frac{y^2}{b^2} + \frac{z^2}{c^2}. \quad (2.60)$$

Eq. (2.59) can be written as

$$1 = \frac{k_x^2}{\frac{2m_x}{\hbar^2}(\varepsilon_F - \varepsilon_{cr})} + \frac{k_y^2}{\frac{2m_y}{\hbar^2}(\varepsilon_F - \varepsilon_{cr})} + \frac{k_z^2}{\frac{2m_z}{\hbar^2}(\varepsilon_F - \varepsilon_{cr})}, \quad (2.61)$$

so one can easily see that a band structure like the one we are dealing with, results in an ellipsoid. By replacing the integral over \mathbf{k} -space in Eq. (2.53) with the volume of the ellipsoid described by Eq. (2.61) yields

$$\begin{aligned} N(\varepsilon_F) &= 2 \cdot \frac{V}{8\pi^3} \cdot \frac{4}{3}\pi \frac{\sqrt{8m_x m_y m_z}}{\hbar^3} \cdot (\varepsilon_F - \varepsilon_{cr})^{3/2} \\ &= \frac{2V}{3\pi^2 \hbar^3} \sqrt{2m_x m_y m_z} (\varepsilon_F - \varepsilon_{cr})^{3/2}. \end{aligned} \quad (2.62)$$

By applying Eq. (2.55), one gets for the DOS of the ellipsoid

$$\delta g(\varepsilon) = \begin{cases} \frac{V}{\pi^2 \hbar^3} \sqrt{2m_x m_y m_z} (\varepsilon - \varepsilon_{cr})^{1/2} & \text{electron ellipsoid} \\ -\frac{V}{\pi^2 \hbar^3} \sqrt{2m_x m_y m_z} (\varepsilon_{cr} - \varepsilon)^{1/2} & \text{hole ellipsoid} \end{cases}. \quad (2.63)$$

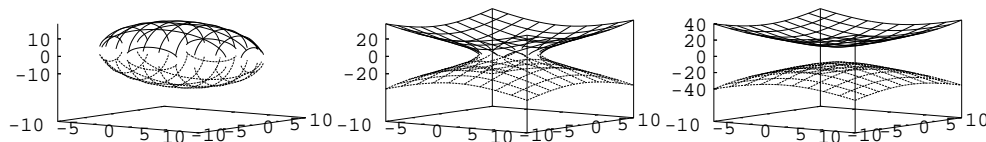


Figure 2.5: Left panel: ellipsoidal Fermi surface. Middle: a neck in the Fermi surface. Right panel: broken neck.

Since the equations derived here are valid for every equi-energy surface and not only for the Fermi surface, the index F was removed from the energy ε .

The DOS here is called δg and not only g to take into account that Eq. (2.63) is not the only contribution to the DOS

$$g(\varepsilon) = g_0(\varepsilon) + \delta g(\varepsilon). \quad (2.64)$$

The part coming from all parts aside from δg of \mathbf{k} -space with energy ε is called g_0 . We are assuming that there are no other ETTs in the energy range under consideration and so $g_0(\varepsilon)$ is a smooth function. Eq. (2.63) is only valid for the argument of the square root being greater than zero. Otherwise $\delta g(\varepsilon) = 0$. Because

$$\lim_{\varepsilon \rightarrow \varepsilon_{cr}} \frac{d\delta g}{d\varepsilon} = 0 \quad (2.65)$$

for ε in the region with no additional ellipsoid and

$$\lim_{\varepsilon \rightarrow \varepsilon_{cr}} \frac{d\delta g}{d\varepsilon} \rightarrow \infty \quad (2.66)$$

for ε in the region with an additional ellipsoid, the DOS has a kink at ε_{cr} , where the ETT takes place.

Necks in the band structure

Now assume that in a certain region of the band structure

$$\varepsilon_n(\mathbf{k}) = \varepsilon_{cr} \pm \left(\frac{\hbar^2}{2m_x} (k_x - k_{0x})^2 + \frac{\hbar^2}{2m_y} (k_y - k_{0y})^2 - \frac{\hbar^2}{2m_z} (k_z - k_{0z})^2 \right) \quad (2.67)$$

is a good approximation. The important difference to Eq. (2.58) is, that the sign of one of the three terms in the bracket differs from the other two. Putting the minus sign in front of the k_z term does not affect generality.

In this case the position of the Fermi energy does not matter, in every case solutions to Eq. (2.51) exist. Those solutions can be written in the form

$$k_z = \pm \sqrt{\frac{m_z}{m_x} k_x^2 + \frac{m_z}{m_y} k_y^2 \mp \frac{2m_z}{\hbar^2} (\varepsilon_F - \varepsilon_{cr})}. \quad (2.68)$$

Here, again we shifted the origin of the coordinate system to the point \mathbf{k}_0 . The first two terms under the square root in Eq. (2.68) are greater or equal zero in any case. The sign of the last term under the square root depends, first on the case, which of the two signs in Eq. (2.67) describes the band under consideration and second, if the energy ε_F is greater or smaller than the critical energy ε_{cr} .

If the third term in Eq. (2.68) is positive, then the square root is real for any value of k_x and k_y . This situation is plotted in Fig. 2.5, right picture. If the third term is negative, then the square root is real only for

$$\frac{m_z}{m_x} k_x^2 + \frac{m_z}{m_y} k_y^2 \geq \left| \frac{2m_z}{\hbar^2} (\varepsilon_F - \varepsilon_{cr}) \right|. \quad (2.69)$$

This means, that for all k_x and k_y values belonging to an ellipse around \mathbf{k}_0 parallel to the xy -plane there does not exist any real k_z value to give the energy ε according to Eq. (2.67). The shape of the equi-energy surface in this case is plotted in the middle panel of Fig. 2.5. This is the so called "neck", which breaks, if the energy is varied so that $\varepsilon_F - \varepsilon_{cr}$ changes sign.

Now we want to calculate the DOS of both, the neck and the broken neck. Like in the case of the ellipsoid we use Eq. (2.53) for this task. For the \mathbf{k} -space integration Eq. (2.68) can be rewritten as

$$1 = \frac{k_x^2}{m_x \left(\frac{k_z^2}{m_z} \pm \frac{2(\varepsilon_F - \varepsilon_{cr})}{\hbar^2} \right)} + \frac{k_y^2}{m_y \left(\frac{k_z^2}{m_z} \pm \frac{2(\varepsilon_F - \varepsilon_{cr})}{\hbar^2} \right)}, \quad (2.70)$$

which is the equation for an ellipse parallel to the xy -plane with size dependent on k_z . And this makes integration easy, because we have only to integrate up all the ellipses:

$$N(\varepsilon_F) = 2 \cdot \frac{V}{8\pi^3} \int_{k_{zmin}}^{k_{zmax}} dk_z \pi \sqrt{m_x m_y} \left(\frac{k_z^2}{m_z} \pm \frac{2(\varepsilon_F - \varepsilon_{cr})}{\hbar^2} \right)$$

$$= \frac{V}{4\pi^2} \sqrt{m_x m_y} \left[\frac{k_z^3}{3m_z} \pm \frac{2(\varepsilon_F - \varepsilon_{cr})k_z}{\hbar^2} \right]_{k_{zmin}}^{k_{zmax}}. \quad (2.71)$$

For an existing neck k_{zmin} and k_{zmax} are just minimal and maximal k_z value of the neck. This yields for the DOS

$$g(\varepsilon) = \pm \frac{V}{2\pi^2} \sqrt{m_x m_y} \frac{(k_{zmax} - k_{zmin})}{\hbar^2}. \quad (2.72)$$

If the neck is broken, we have two integration ranges: from k_{zmin} to that k_z value, where the area of the ellipse reaches zero

$$0 = \frac{k_z^2}{m_z} \pm \frac{2(\varepsilon_F - \varepsilon_{cr})}{\hbar^2} \quad (2.73)$$

$$\Leftrightarrow k_z = \pm \frac{\sqrt{2m_z|\varepsilon_F - \varepsilon_{cr}|}}{\hbar} \quad (2.74)$$

and from the other k_z value, where the area of the ellipse reaches zero to k_{zmax} . We get

$$N(\varepsilon_F) = \frac{V}{4\pi^2} \sqrt{m_x m_y} \left(\frac{k_{zmax}^3 - k_{zmin}^3}{3m_z} \pm \frac{2(\varepsilon_F - \varepsilon_{cr})(k_{zmax} - k_{zmin})}{\hbar^2} \right. \\ \left. - \left(\frac{2(2m_z|\varepsilon_F - \varepsilon_{cr}|)^{3/2}}{3m_z\hbar^3} \pm \frac{4(\varepsilon_F - \varepsilon_{cr})\sqrt{2m_z|\varepsilon_F - \varepsilon_{cr}|}}{\hbar^3} \right) \right). \quad (2.75)$$

This leads to the following DOS:

$$g(\varepsilon) = \pm \frac{V}{2\pi^2} \sqrt{m_x m_y} \frac{(k_{zmax} - k_{zmin})}{\hbar^2} + \delta g(\varepsilon) \quad (2.76)$$

with

$$\delta g(\varepsilon) = \begin{cases} -\frac{V}{\pi^2\hbar^3} \sqrt{2m_x m_y m_z} (\varepsilon_{cr} - \varepsilon)^{1/2} & + \text{sign in Eq. (2.67)} \\ \frac{V}{\pi^2\hbar^3} \sqrt{2m_x m_y m_z} (\varepsilon - \varepsilon_{cr})^{1/2} & - \text{sign in Eq. (2.67)} \end{cases}. \quad (2.77)$$

Comparing all the results (additional ellipsoid, no additional ellipsoid, neck, broken neck) leads to the conclusion, that in case of an ETT the DOS can be written like in Eq. (2.64) with

$$|\delta g(\varepsilon)| = \begin{cases} \frac{V}{\pi^2\hbar^3} \sqrt{2m_x m_y m_z} |\varepsilon - \varepsilon_{cr}|^{1/2} & \text{Region I} \\ 0 & \text{Region II} \end{cases}. \quad (2.78)$$

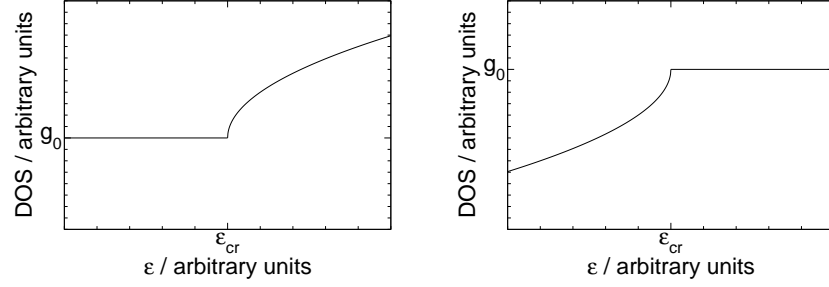


Figure 2.6: Left picture: DOS for an electron ellipsoid appearing at ε_{cr} or DOS of a neck, whose band structure has two terms with a minus sign in front, breaking at $\varepsilon = \varepsilon_{cr}$. Right picture: DOS for an hole ellipsoid disappearing at $\varepsilon = \varepsilon_{cr}$ or DOS of a neck, whose band structure has one term with a minus sign in front and being created at $\varepsilon = \varepsilon_{cr}$.

Here, region I is the less connected region (one ellipsoid more in the Fermi surface or a broken neck) and in region II the neck is connected and the ellipsoid has vanished or not yet formed. The shape of the DOS, which has a kink at the transition due to the additional contribution on one side, is plotted in Figure 2.6. For simplicity g_0 has been assumed constant in these plots¹.

For we have connected Lifshitz transitions to special shapes of the band structure, the conclusion can be drawn, that Lifshitz transitions can already be seen in the band structure. If a minimum (maximum) of the band structure crosses the Fermi energy, an additional electron (hole) ellipsoid will appear on that side of the transition, where additional solutions to Eq. (2.51) exist. In the case of a Lifshitz transition, which creates or disrupts a neck, a saddle-point crosses the Fermi level.

So in general one can say, that if

$$\frac{\partial \varepsilon_n(\mathbf{k})}{\partial \mathbf{k}} = 0 \quad (2.79)$$

is fulfilled for some band at the Fermi energy, the material is undergoing a Lifshitz transition.

Note, that Lifshitz transitions most likely appear on symmetry lines of

¹For the connection between band structure, Fermi surface and DOS in other special cases see [19].

the BZ because due to symmetry constraints Eq. (2.79) has to be fulfilled there. But this does not exclude the possibility of a Lifshitz transition appearing at a point of the BZ, which is not distinguished by symmetry.

2.3.4 *Anomalies of thermodynamic and other quantities induced by an ETT*

To see the consequences of the van Hove singularity in the thermodynamic quantities, we calculate the thermodynamic potential $\Omega(\mu, T)$ of an electron gas in a metal. The thermodynamic potential is defined as

$$\Omega = U - TS - \mu N. \quad (2.80)$$

Here, U is the inner energy of the system, T denotes the temperature, S the entropy, μ the chemical potential and N the particle number. We consider here only the case $T = 0$. In this case the energy of the system is given by

$$U = \int_{-\infty}^{\varepsilon_F} d\varepsilon g(\varepsilon) \varepsilon \quad (2.81)$$

and the particle number by Eq. (2.52). At zero temperature the chemical potential equals the Fermi energy:

$$\mu(T = 0) = \varepsilon_F. \quad (2.82)$$

This yields for the thermodynamic potential

$$\Omega(\varepsilon_F, 0) = \int_{-\infty}^{\varepsilon_F} d\varepsilon (\varepsilon - \varepsilon_F) g(\varepsilon). \quad (2.83)$$

If we write $g(\varepsilon)$ like in Eq. (2.64), we can calculate

$$\delta\Omega = \int_{-\infty}^{\varepsilon_F} d\varepsilon (\varepsilon - \varepsilon_F) \delta g(\varepsilon). \quad (2.84)$$

Again, considering only the case of an additional electron surface, one gets for Region I

$$\begin{aligned} \delta\Omega &= \frac{V}{\pi^2 \hbar^3} \sqrt{2m_x m_y m_z} \int_{\varepsilon_{cr}}^{\varepsilon_F} d\varepsilon (\varepsilon - \varepsilon_F) (\varepsilon - \varepsilon_{cr})^{1/2} \\ &= -\frac{4}{15} \frac{V}{\pi^2 \hbar^3} \sqrt{2m_x m_y m_z} (\varepsilon_F - \varepsilon_{cr})^{5/2} \end{aligned} \quad (2.85)$$

and for Region II

$$\delta\Omega = 0. \quad (2.86)$$

If we consider $\Omega(\varepsilon_F, 0)$ and its derivatives, we find that $\Omega(\varepsilon_F, 0)$ and $\partial\Omega/\partial\varepsilon_F$ are differentiable, $\partial^2\Omega/\partial\varepsilon_F^2$ is continuous but not differentiable at $\varepsilon_F = \varepsilon_{cr}$ due to its vertical kink, which is proportional to $(\varepsilon_F - \varepsilon_{cr})^{1/2}$ and $\partial^3\Omega/\partial\varepsilon_F^3$ tends to infinity at $\varepsilon_F = \varepsilon_{cr}$ proportional to $(\varepsilon_F - \varepsilon_{cr})^{-1/2}$. These considerations lead Lifshitz to call the topological transition of a Fermi surface $2\frac{1}{2}$ order phase transition [5] though an ETT can only be considered as a phase transition at $T = 0$. At higher temperatures the transition is smeared out.

For thin layers or nanowires one may have a two or one dimensional Fermi surface. In these cases the dependence of $N(\varepsilon)$, $g(\varepsilon)$ and $\Omega(\varepsilon_F, 0)$ differs from the three dimensional case calculated above. In one dimension the Fermi surface is a line and the only topological change, which is possible, is the occurrence of new lines or the disappearance of lines. The case with the neck is not possible in one dimension. In two dimensions ellipses can appear or disappear and the creation or disruption of a neck is possible. But the last case (neck) is degenerated since the breaking of a neck of one kind of charge carriers (e. g. electrons) in two dimensions creates a neck turned by 90 degrees of the other kind of charge carriers (in this example holes), which is shown in Figure 12 of Ref. [6].

A consequence of the transition in three dimensions between open and closed orbits, which may happen when necks are created or disrupted, can be seen in the electrical resistance in strong magnetic fields. The electrical resistance in strong magnetic fields depends on the existence of open orbits. If there are no open orbits, the electrical resistance tends to saturate for $\mathbf{B} \rightarrow \infty$. If there are open orbits, the electrical resistance grows without limit with growing magnetic field (for the derivation of this finding see [18]).

Chapter 3

RESULTS

3.1 ISOMORPHIC VOLUME COLLAPSE OF YCo_5 UNDER PRESSURE

For designing new magnetic materials it is important to know, which property of a compound is due to which property of the constituting atoms or to which interaction between atoms. In this sense YCo_5 is a very interesting compound because it is the parent compound of the important class of 1–5 rare earth transition metal compounds (RT_5) to which for example the important magnetic compound SmCo_5 belongs to. In exploring YCo_5 one can find out, which properties of the RCo_5 are due to the rare earth 4f electrons and which come from Co because Y is non-magnetic and so all magnetic properties of YCo_5 are determined by Co. In SmCo_5 the situation is not so easy because there both kinds of constituting atoms are magnetic.

Since the end of the sixties [20, 21] much work has been devoted to YCo_5 (see Table 36 and Table 37 in Ref. [13] for publications considering YCo_5). For example Yamada *et al.* [22] considered the pseudo-binary compound $\text{Y}(\text{Co},\text{Ni})_5$ and suggested the existence of a low moment phase in YCo_5

at a reduced unit-cell volume. This gave the motivation for our work because from this we expected effects like anomalies of volume or anomalies of elastic properties.

We computed total energy, magnetic moment, band structure and DOS of YCo_5 at various unit cell volumes, which correspond to different pressures. Assuming no structural change to occur, we found, that YCo_5 undergoes a volume collapse at about 6 GPa with respect to the zero pressure volume LDA yields or at about 21 GPa with respect to the larger zero pressure volume measured in experiment. This volume collapse then was experimentally confirmed to be isomorphic [7].

Isomorphic volume collapse is a rare phenomenon. Most isomorphic volume collapses known until now happen in cubic materials like SmS [23] and Ce [24, 25]. In the case of Ce the mechanism of the transition is still debated [26, 27], more than 50 years after its discovery.

To the best of our knowledge no hexagonal isomorphic transition was found before this work. Here, in contradiction to the transition in Ce , at first the mechanism was understood and the volume collapse was predicted and then the measurements, which confirmed our prediction were done [7].

This chapter is constructed like follows: In Section 3.1.1 the structure of YCo_5 is explained. Section 3.1.2 contains details about the calculations, while Section 3.1.3 comprises some remarks about the convergence of parameters. The results on fixed spin moment calculations are discussed in Section 3.1.4, whereas Section 3.1.5 contains results about the magnetic moment of YCo_5 under pressure. In Section 3.1.6 the volume collapse is found and Section 3.1.7 details the behavior of lattice constants under pressure. The extension of the calculations down to the unit cell volume where YCo_5 becomes non-magnetic is shown in Section 3.1.8. Section 3.1.9 displays the band structure and DOS of YCo_5 . The pressure induced changes of the Fermi surface in YCo_5 are shown in Section 3.1.10. Finally Section 3.1.11 concludes the chapter about YCo_5 and summarizes the most important results.

3.1.1 Structure of YCo_5

YCo_5 crystallizes in the hexagonal CaCu_5 structure (P6/mmm, space group 191, see Figure 3.1) with a c/a ratio of 0.810(4) under ambient conditions, with $a = 4.940(7)$ Å and $c = 4.000(16)$ Å [28, 29]. The unit cell contains six atoms, which are sitting on three different Wyckoff positions. The Y atom is placed in the corners of the unit cell on a $1a$ position, two of the Co atoms

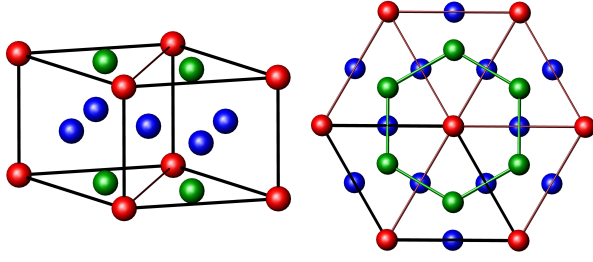


Figure 3.1: The picture on the left shows the unit cell of YCo_5 containing six atoms. The red balls depict the Y-atoms and the blue and green balls depict the Co-atoms. Different colors denote different Wyckoff-positions. The picture on the right shows a view along the c -axis with some neighboring atoms added to emphasize the hexagonal structure ($P6/mmm$, Space group 191).

are occupying $2c$ positions. They share the same plane with the Y atoms, each in the middle of a triangle spanned by the Y atoms. The third Wyckoff position ($3g$) is occupied by three Co atoms at the centers of rectangles of neighboring Y atoms.

3.1.2 Method of calculation

The calculations were performed with FPLO [4], release 3. For the Y-basis we considered $1s2s2p3s3p3d$ as core states, $4s4p$ as semi-core, which means that they are fully occupied shells, that are included in the valence basis, which are more extended than half of the nearest neighbor distance. $5s5p4d$ are taken as normal valence states and the $5d$ state was added for basis completeness (such states we call "polarization states"). For the Co-basis we use $1s2s2p$ as core, $3s3p$ as semi-core, $4s4p3d$ as valence and $4d$ as a polarization state. A k -mesh subdivision of $36 \times 36 \times 36$ was used (2413 k -points in the irreducible part of the BZ). With this setting we tested the convergence, calculated the Fixed Spin Moment (FSM) results, the DOS and all calculations with c/a fixed.

For the calculations with relaxed c/a and for the band structure we used a somewhat different setting of $30 \times 30 \times 30$ k -points (1456 k -points in the irreducible part of the BZ). In the basis only the polarization states differ. This time we have taken $4f$ instead of $5d$ as a polarization state for the Y-atoms. For the Co-atoms we used both, $4d$ and $4f$ as polarization states.

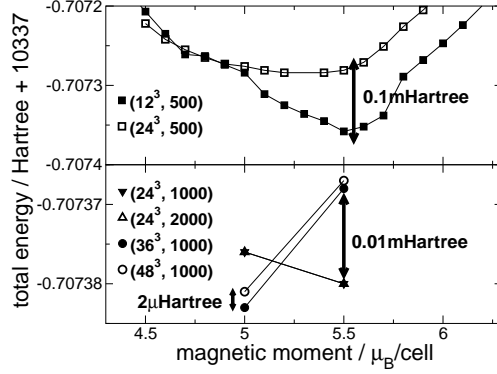


Figure 3.2: Convergence test regarding \mathbf{k} -point sampling and Fourier components of the Ewald potential. Total energies are shown, obtained by fixed spin moment calculations at a unit cell volume of 73 \AA^3 and $c/a = 0.810$. The symbols denote a pair of parameters (\mathbf{k} -points in the full BZ; components of the Ewald potential) as indicated in the legends.

We used 1000 Fourier components of the Ewald-potential. All calculations have been done scalar relativistic. For the exchange-correlation potential we used the local spin density approximation (LSDA) in the version of Perdew Wang 92 [30].

3.1.3 Convergence of parameters

We performed calculations with different basis-sets, various numbers of \mathbf{k} -points and Fourier components of the Ewald potential and varied some other parameters of the code to check the convergence and accuracy of the results. For a given setting of parameters, the energy convergence of the self-consistent runs was better than 10^{-7} Hartree.

In Figure 3.2 the convergence regarding \mathbf{k} -points and Fourier components of the Ewald potential is shown. In the upper panel one can see, that the $E(M)$ -curve is much more smooth if one increases the number of \mathbf{k} -points in the full BZ from 12^3 to 24^3 . In the lower panel the full curve is not calculated, only two points of the $E(M)$ -curve are calculated to study the convergence behavior. If one compares the points calculated with 24^3 \mathbf{k} -points but one time with 1000 Fourier components of the Ewald potential and the other time with 2000 Fourier components of the Ewald potential,

one can see that the difference between the two is well below $1\mu\text{Hartree}$. Therefore we concluded, that 1000 Fourier components of the Ewald potential are sufficient. Comparing the points calculated with 1000 Fourier components of the Ewald potential and 36^3 versus 48^3 \mathbf{k} -points in the full BZ, one finds that the difference in energy is about $2\mu\text{Hartree}$ or less. So we concluded that 36^3 \mathbf{k} -points are sufficient for an accurate calculation.

3.1.4 Fixed Spin Moment calculations

Recent calculations of the volume dependent magnetic moment of YCo_5 by Yamada *et al.* [22] hint at two different possible magnetic states, one with a higher magnetic moment (in the following called "high spin (HS) state") and one with a lower magnetic moment (in the following called "low spin (LS) state"). To verify this finding and to find out, if solutions with a different magnetic moment occur for the same volume and c/a ratio, we carried out FSM calculations [31]. All FSM calculations were done at a fixed c/a ratio of 0.81, but for different volumes. The results are displayed in Figure 3.3 in comparison with the original data by Yamada *et al.*.

The different curves show the spin moment dependence of total energy for different volumes. The left graph of Figure 3.3 shows our calculations and the right part of the figure is taken from Ref. [22]. It is obvious, that there is qualitative agreement between both calculations. In particular, the shapes of the $E(M)$ -dependence are very similar. In both calculations there is a HS state for large volumes at a magnetic moment between 6 and $7\mu_{\text{B/cell}}$ and for smaller volumes a broader minimum at a lower magnetic moment. Both find a region of coexistence between HS and LS states but in our calculations this region lies between 73.0 \AA^3 and 73.3 \AA^3 and in the calculations of Yamada *et al.* ([22]) this region lies around $V = 75.0\text{ \AA}^3$.

These considerable quantitative differences are also visible in Figure 3.4 discussed below. These quantitative differences are due to several technical differences between the two distinct calculations. First, Yamada *et al.* have used an Linear Muffin-Tin Orbital (LMTO) - Atomic Sphere Approximation (ASA) method which is not as accurate as recent full-potential codes. Furthermore, they have chosen a somewhat different c/a ratio of $\sqrt{2/3} \approx 0.816$ and they have used another exchange-correlation potential (von Barth and Hedin) than applied in the present work.

Please note, that the scaling of both parts of Figure 3.3 is different, since

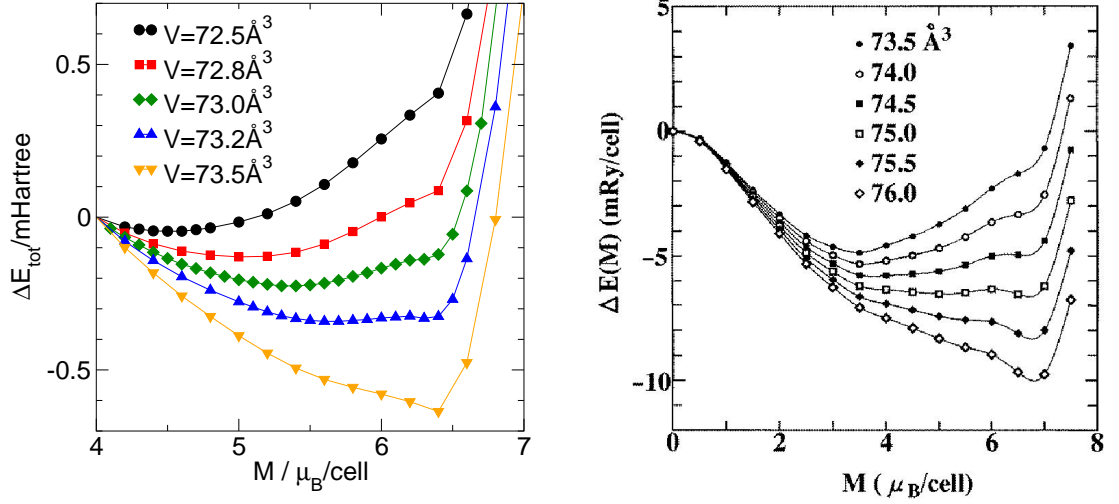


Figure 3.3: Results of FSM calculations for YCo_5 . Total energy differences are plotted against the magnetic moment for different volumes. The left panel shows our results and the right panel is taken from Ref. [22]. Please note the different energy and moment scales. In the left panel, all curves are shifted to coincide at a magnetic moment of $4 \mu_{\text{B}}/\text{cell}$. In the right panel, they are shifted to coincide at zero moment.

we aimed at a higher resolution within the transition region and present results from a more narrow range of volumes and moments. Let us first concentrate on the lowest curve in the left graph (yellow triangles): It belongs to a volume of 73.5 \AA^3 , the largest volume displayed in this figure. It has one minimum, which is deep and sharp, at a magnetic moment of about $6.4 \mu_{\text{B}}/\text{cell}$. The next lowest curve (blue triangles, $V = 73.2 \text{ \AA}^3$) exhibits two minima, nearly degenerate in energy, one at about $5.5 \mu_{\text{B}}/\text{cell}$ (LS state) and the other at about $6.3 \mu_{\text{B}}/\text{cell}$ (HS state). The minimum of the LS state is much broader than the minimum of the HS state. Going to even smaller volumes ($V = 73.0 \text{ \AA}^3$, green diamonds), one finds that the LS state becomes the global minimum and the HS state becomes metastable and eventually unstable ($V = 72.8 \text{ \AA}^3$, red squares, and $V = 72.5 \text{ \AA}^3$, black circles). So we indeed found two solutions in the region $73.0 \text{ \AA}^3 \leq V \leq 73.3 \text{ \AA}^3$.

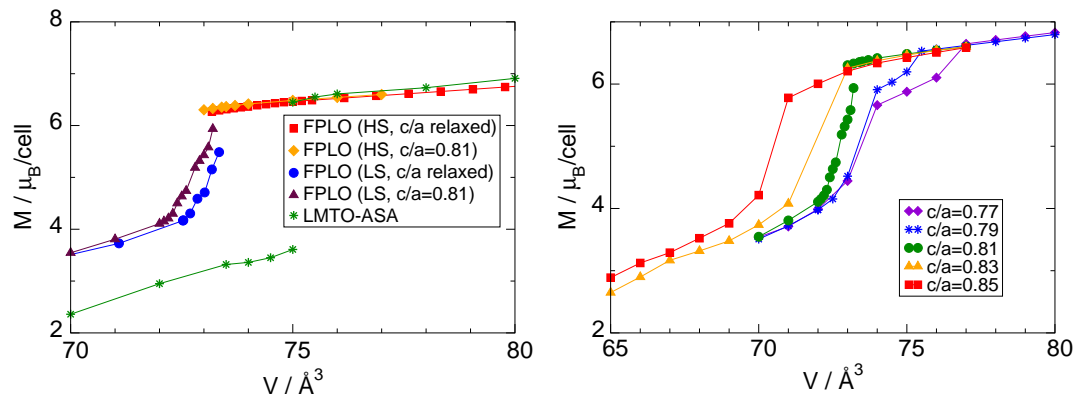


Figure 3.4: Left panel: magnetic moment per unit cell against volume. The green stars show LMTO-ASA calculations taken from Ref. [22]. The other symbols denote our FPLO calculations. Right panel: magnetic moment plotted against volume of the unit cell for different c/a ratios.

3.1.5 The magnetic moment of YCo_5 under pressure

To find out, how the magnetic moment changes with pressure, we carried out DFT calculations without fixing the moment. The magnetic moment has been calculated for various volumes and different c/a ratios. The results are shown in Figure 3.4, where the magnetic moment is displayed against volume. In the left panel results of three different sets of calculations are shown: In the first set, the c/a ratio was fixed at 0.81 (yellow diamonds and violet triangles). The second set of calculations was done with relaxed c/a . The results of these calculations are marked with red squares and blue circles. The third displayed set (green stars) are results by Yamada *et al.* taken from Ref. [22].

Comparing the different HS results (red squares, yellow diamonds and the upper line of the green stars), one finds that all calculations yield the same weak volume dependence of magnetic moment. This insensitivity of spontaneous magnetization with respect to both pressure and calculational details can be understood from the strong (saturated) ferromagnetic state of YCo_5 at ambient or low-pressure conditions. This point will be detailed further in Section 3.1.9.

At a volume $V = 75 \text{\AA}^3$ Yamada *et al.* [22] find, that the magnetic moment suddenly jumps down from a value of about $6.45 \mu_B/\text{cell}$ to approximately

$3.6 \mu_{\text{B}}/\text{cell}$. Our calculations also yield such a transition but in the volume range $73.0 \text{ \AA}^3 \leq V \leq 73.3 \text{ \AA}^3$ and we find a much smaller moment jump. Instead we find a steep decrease of the magnetic moment between $V = 73.3 \text{ \AA}^3$ and $V = 72.0 \text{ \AA}^3$ not observed by Yamada *et al.* [22]. For volumes smaller than $V = 72 \mu_{\text{B}}/\text{cell}$ the magnetic moment is slowly decreasing with decreasing volume. The slope of the magnetic moment dependence on volume is roughly the same in our data compared with the data by Yamada *et al.* [22] but in our results the magnetic moment is about $1 \mu_{\text{B}}/\text{cell}$ larger than in the data by Yamada *et al.* [22].

We have displayed both the stable and the metastable solution within the narrow volume range of coexistence. Since both branches of solutions do not merge even if the c/a ratio is relaxed, the transition between HS and LS states is of first order. The existence region of the low moment state is shifted to a somewhat larger volume in the case of relaxed c/a ratio in comparison with $c/a = 0.81$.

The resulting magnetic moments for the calculations with different volumes and different c/a ratios are shown in the right panel of Figure 3.4. In the HS state, all c/a ratios yield about the same magnetic moment for each volume and the magnetic moment is slowly decreasing with volume. The transition occurs for every c/a ratio at a different volume. At first the smallest c/a ratio undergoes the transition and then the larger ones follow. In the low moment phase the difference in magnetic moments between different c/a ratios for the same volume is much more pronounced than for saturated moments. For c/a ratios smaller than $c/a = 0.80$ there is directly after the transition a strange kink in the $M(V)$ -curve, not observed for $c/a > 0.80$. This kink is due to small peaks in the DOS.

The change of the magnetic moments of the individual atoms at the different Wyckoff positions with hydrostatic pressure, i.e., the volume dependence with relaxed c/a ratio, is shown in Figure 3.5. In the saturated spin state all Co atoms carry the same moment of about $1.4 \mu_{\text{B}}/\text{atom}$ though they occupy different Wyckoff positions. At the transition the magnetic moment of those Co atoms which occupy the 3g Wyckoff position is decreasing much stronger (by about $0.7 \mu_{\text{B}}/\text{atom}$) than the moment of those atoms occupying Wyckoff position 2c (by about $0.4 \mu_{\text{B}}/\text{atom}$). The Y atoms carry a small negative moment, which is roughly proportional to the total Co moment.

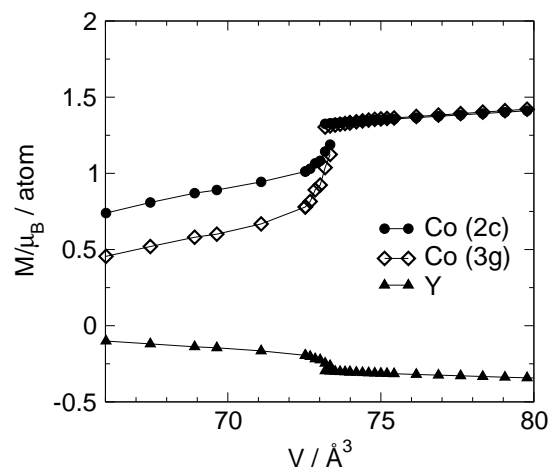


Figure 3.5: Magnetic moment per atom against volume.

3.1.6 Lattice geometry and elastic anomaly under pressure

We discussed in Section 2.2.1, that hydrostatic conditions have to be modeled by relaxation of c/a for every given volume. The dependence of the relaxed c/a ratio on volume is shown in Figure 3.6. In this plot the direction of the V -axis is inversed, so that pressure is increasing from left to right. With decreasing volume the c/a ratio shows a linear increase in the HS state. At the transition to the LS state the c/a ratio jumps to a lower value, which is close to the ideal c/a ratio of YCo_5 ¹ and then resumes to increase linearly.

In Figure 3.7 the total energy (for relaxed c/a) is plotted against the volume of the unit cell. The red squares (blue circles) denote the HS (LS) state. On the coarse scale of the left panel it is hard to distinguish two different parabolas. Since we are especially interested in the transition region, we zoomed into that region in the right panel. The rectangle in the left panel marks the location of the zoomed area. In the magnification, the coexistence region (around 73.2 Å^3) of the HS and the LS solutions is displayed. Both states are degenerate in this region, but the curvature of $E(V)$ differs. This is obvious from the linear and quadratic fits to the data points of HS and LS states, respectively. The LS data are almost equally well described by both

¹To calculate the ideal c/a ratio of YCo_5 , which amounts to $\sqrt{95/147}$, Y- and Co-atoms had been considered as hard spheres, where the radius of Co has been assumed to be $3/4$ of the radius of Y. c and a in units of the radius of the Y-atom had been adjusted such that for the two smallest distances between two atoms in the unit cell the atoms touch.

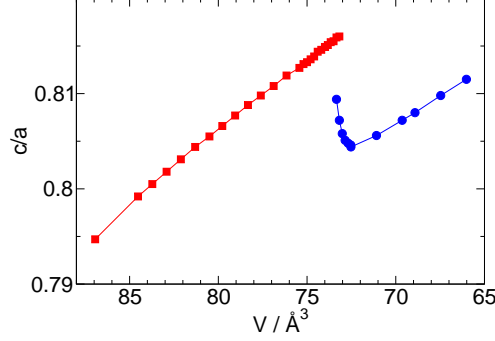


Figure 3.6: Dependence of the relaxed c/a ratio on volume. The red squares denote the HS branch, the blue bullets denotes the LS branch.

fits in the magnified region, while the HS data show a visible deviation from the linear fit.

It is obvious from the presented data (Figs. 3.4-3.6) that there is no continuous transformation between HS and LS states, i.e., a first order transition will take place. In order to evaluate the related transition pressure, we calculated the enthalpies $H(P)$ of both states, Figure 3.8. Both branches show almost the same dependence on pressure (P , left panel of Figure 3.8). To visualize their crossing point, we have subtracted a linear term and present $H/\text{Hartree} + 10337 - 0.0169992 \cdot P/\text{GPa}$ in the right panel.

When looking on the enthalpy-pressure plot $H(P)$, Figure 3.8, one finds the transition at that pressure P_{cr} and enthalpy H_{cr} where the LS enthalpy-pressure function $H_{LS}(P)$ and the HS enthalpy-pressure function $H_{HS}(P)$ cross. In each of the phases to the enthalpy H_{cr} and the pressure P_{cr} there is a volume belonging to this point in the enthalpy-pressure plane. This volume differs from one phase to the other. This means that the volume jumps from $V_{HS}(H_{cr}, P_{cr})$ to $V_{LS}(H_{cr}, P_{cr})$.

We calculated $V_{HS}(H_{cr}, P_{cr}) = (73.8 \pm 0.1) \text{ Å}^3$ and $V_{LS}(H_{cr}, P_{cr}) = (72.8 \pm 0.2) \text{ Å}^3$. The relative change in volume is about 1.4%. From Figure 3.6 one reads the corresponding c/a ratios: $(c/a)_{HS} = 0.815 \pm 0.0005$ and $(c/a)_{LS} = 0.805 \pm 0.001$. This means that the region, where the magnetic moment has its steep decrease is metastable and in reality the system should jump over it.

From the left panel of Figure 3.8 one can read that the transition pressure

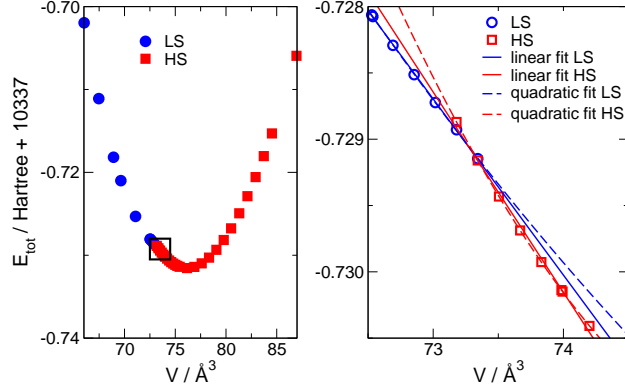


Figure 3.7: Total energy of YCo_5 in dependence of the unit cell volume. Red squares (blue circles) denote the HS (LS) spin state. The left panel shows an overview and the right panel shows a magnification of the transition region, marked by the rectangle in the left panel. Linear and quadratic fits to the HS and LS data points are included in the right panel. Only the data within the displayed region were used for the fitting.

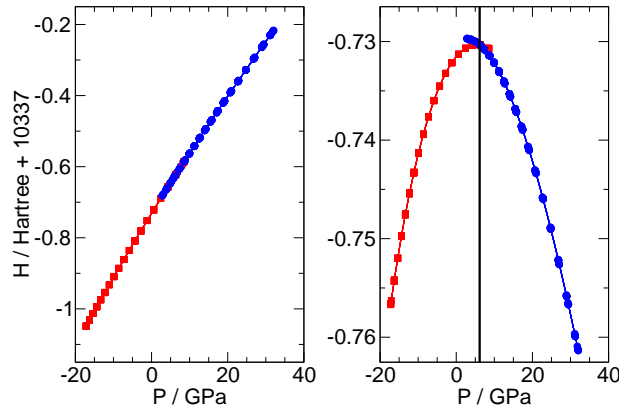


Figure 3.8: Enthalpy versus pressure (left panel) and non-linear contributions to the enthalpy (see text) versus pressure (right panel) to visualize the transition. Red squares (blue circles) denote HS and LS states, respectively.

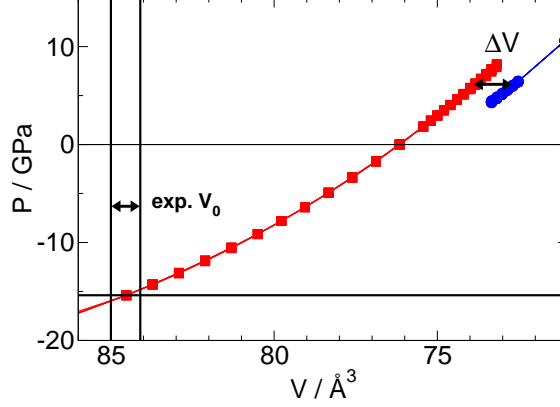


Figure 3.9: Hydrostatic pressure against volume. Zero pressure refers to the LSDA equilibrium volume. Red squares denote HS data and blue circles denote LS data. Two values of experimental volumes [28] are indicated (vertical lines). The horizontal line close to -15 GPa refers to the experimental pressure zero. The volume jump at the transition is indicated.

is about 6 GPa. The calculated transition pressure is much lower than the measured one because the zero pressure volume of LDA is much smaller than the experimental zero pressure volume ($V_{LDA} = 76.2 \text{ \AA}^3$, $V_{exp} \approx 85 \text{ \AA}^3$), so less pressure is needed to compress it to the transition volume. If one would calculate the transition pressure as the pressure difference between $V = 85 \text{ \AA}^3$ and $V = 73 \text{ \AA}^3$, one would arrive at a transition pressure of about 21 GPa (see Figure 3.9) which is in agreement with experiment, where the transition happened at a pressure of 19 GPa [7].

The correspondence between volume and pressure in the hydrostatic case is shown in Figure 3.9. With increasing pressure the volume becomes smaller until the transition takes place. At the transition the volume jumps at a certain pressure down to a lower value and smoothly decreases further. The region of coexistence, where we found a HS and a LS solution for the same volume is clearly seen in this plot. (The data were divided into HS data and LS data and the equation of state [32] was applied separately to both phases.)

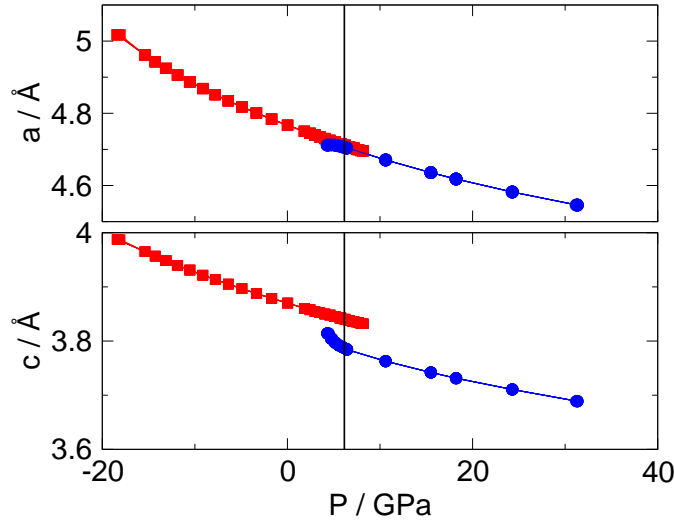


Figure 3.10: Upper panel: lattice constant a versus pressure. Lower panel: lattice constant c versus pressure. Red squares denote HS data and blue circles denote LS data. The vertical line shows the theoretically estimated transition pressure.

3.1.7 Behavior of lattice constants under pressure

When hydrostatic pressure is applied to the sample the c/a ratio increases until the transition is reached. At the transition it jumps back to a smaller c/a ratio and then continues increasing (compare Figure 3.6). This means that the c -axis and the a -axis are differently affected by pressure, what is shown in Figure 3.10. The lattice constants decrease with increasing pressure. The transition pressure is marked with a vertical line. The upper panel shows, that the lattice constant a decreases smoothly with pressure. The points below the smooth curve for pressures slightly lower than the transition pressure are some metastable solutions from the region of the steep decrease of the magnetic moment.

The lower panel of Figure 3.10 shows the lattice constant c versus pressure. It is obvious that the volume collapse at the transition is induced by the collapse of the lattice constant c . This lattice constant decreases smoothly with pressure for pressures smaller than the transition pressure. When the transition pressure is reached, c suddenly shrinks from 3.84 Å to 3.78 Å and then it again decreases smoothly with increasing pressure.

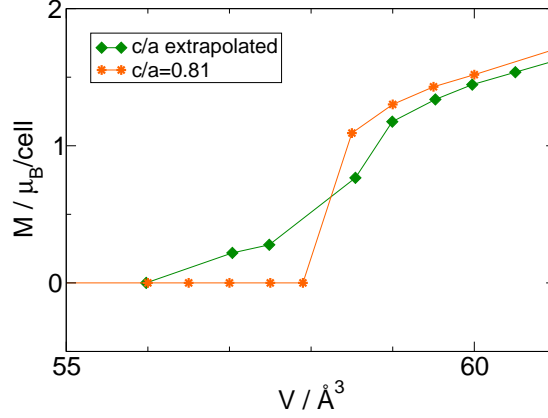


Figure 3.11: Transition to a non-magnetic state. The orange stars denote calculations with a c/a ratio fixed at 0.81 and the green diamonds denote calculations with an extrapolated relaxed c/a ratio.

3.1.8 Transition to non-magnetic state

Looking at Figure 3.4 one can see that after the transition the magnetic moment continues to decrease with decreasing volume. So there must be a pressure and a corresponding volume at which the magnetic moment vanishes (compare discussion in Chapter 2.2.3). To find the pressure and the corresponding volume at which the magnetic moment vanishes, the calculations were extended down to very small volumes. Because it requires much calculation time to relax the c/a ratio for every volume, for these calculations at first the c/a ratio was kept fixed at $c/a = 0.81$ to estimate the volume at which YCo_5 becomes non-magnetic and then the $(c/a)(V)$ curve (Figure 3.6) was extrapolated. Figure 3.11 shows the volume dependence of the magnetic moment both for $c/a = 0.81$ and for the extrapolated c/a ratio. The calculations show that the transition from magnetic to non-magnetic state takes place at a volume between 56 \AA^3 and 58.5 \AA^3 .

This volume range corresponds to an approximate pressure range between 80 and 110 GPa (in experiment it should be about 15 GPa higher). The total energy is convex in the considered volume range, i.e., the transition to the non-magnetic state is at least of second order.

3.1.9 Band structure and DOS of YCo_5

YCo_5 has a very interesting band structure shown in Figure 3.12. Interesting, because it has two flat bands in the spin-up part of the band structure: one has no dispersion in c -direction (flat band between Γ and A), therefore it is flat in one dimension and the other is dispersion-less in the hexagonal plane (flat band along Γ -M-K- Γ), that means it is flat in two dimensions. In equilibrium (zero pressure, upper panel of Figure 3.12) these flat bands lie below the Fermi energy: they are fully populated. With increasing pressure the flat bands approach the Fermi level. At first, the flat band between Γ and A crosses the Fermi level. The transition takes place when the two-dimensional flat band jumps over the Fermi level. At higher pressures than the transition pressure the flat bands are empty at zero temperature (lower panel of Figure 3.12).

As a band-weight calculation show, only the Co 3d states contribute to the flat bands. Such flat bands make very sharp peaks in the DOS, which is plotted in Figure 3.13. The peak in the spin-up part of the DOS right below the Fermi level in the HS case and right above the Fermi level (LS case) is the upper band edge of the Co 3d band. As explained in the last paragraph, in the HS state the Co 3d band is fully populated whereas in the LS state, due to the broadening of the bands under pressure, its upper band edge, where the peak is situated, crosses the Fermi level and thus the band becomes partially depopulated. The magnetism of materials with a fully populated 3d band is called "strong ferromagnetism" and the magnetism of materials with a partly depopulated 3d band is called "weak ferromagnetism" (see Chapter 2.2.2. of Ref. [33]). So the observed transition in YCo_5 can be seen as a *transition from strong to weak ferromagnetism*.

3.1.10 The Fermi surface of YCo_5

To see if there are Lifshitz transitions taking place in YCo_5 , the Fermi surface was calculated at four different volumes: at the theoretical zero pressure volume ($V = 76.16 \text{ \AA}^3$), at volumes somewhat larger and somewhat smaller than the transition volume ($V = 73.83 \text{ \AA}^3$, $V = 72.53 \text{ \AA}^3$, respectively.) and at a very small volume of about $V = 67.47 \text{ \AA}^3$. The Fermi surface of YCo_5 is beautiful but complicated, which can be seen in Figures 3.14, 3.15 and 3.16. Figure 3.14 shows the spin-up part of the Fermi surface. The first row shows the spin-up part of the Fermi surface for the largest of the four

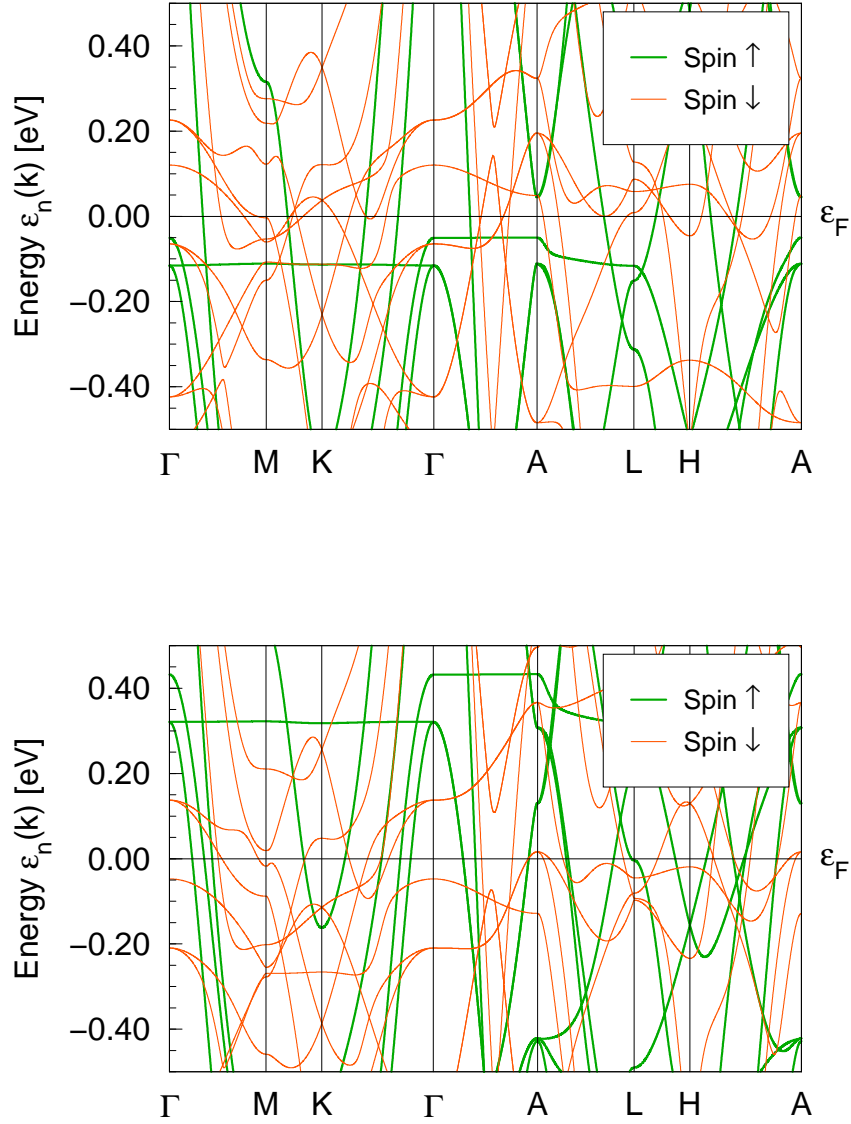


Figure 3.12: Upper panel: band structure of YCo₅ around the Fermi energy at zero pressure. Lower panel: band structure of YCo₅ around the Fermi energy for $V = 72.53 \text{ \AA}^3$, $c/a = 0.80376$. One can see that the flat band in the hexagonal plane (Γ -M-K- Γ) is below the Fermi level at zero pressure and above it for pressures higher than the transition pressure.

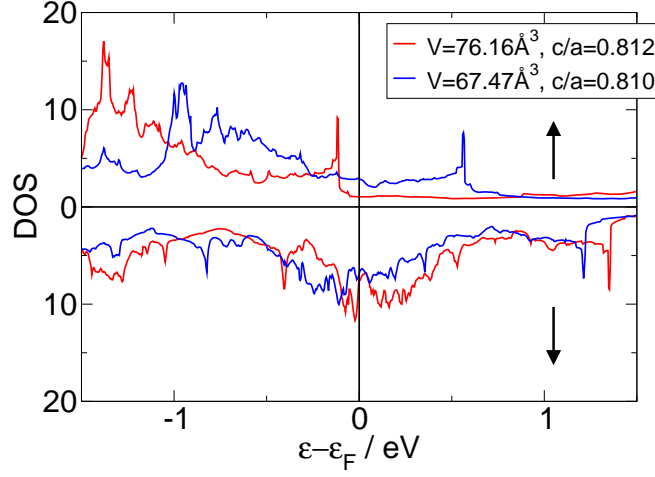


Figure 3.13: Total DOS plotted for both spin channels. The red curve belongs to YCo_5 in the HS case and the blue curve shows the total DOS in the LS case.

calculated volumes, the second row the second largest and so on. It can be seen that there are several Lifshitz transitions taking place, not only at the first-order transition, but also within the HS phase and the LS phase. In the HS phase, between the theoretical zero pressure volume and the transition volume there is a new hole surface appearing and in addition a neck is created. Furthermore, in the LS phase there are new hole surfaces appearing in band number 48 and in band number 49 and 50 a lot of necks are created and new parts of the Fermi surface appear.

So what is special at the transition? If one compares the pictures within each column (each column represents one band), one easily observes, that the Fermi surface sheets in the same column show similarities with the other Fermi surface sheet belonging to the same phase but if one compares the Fermi surface sheets of the same band before and after the transition there is not much similarity left. In the LS phase there are two bands intersecting the Fermi level, which do not intersect with the Fermi level in the HS phase and one band, which has intersections with the Fermi level in the HS phase do not cross the Fermi level in the LS phase anymore. In addition those two bands which remain at the Fermi energy at volumes on both side of the

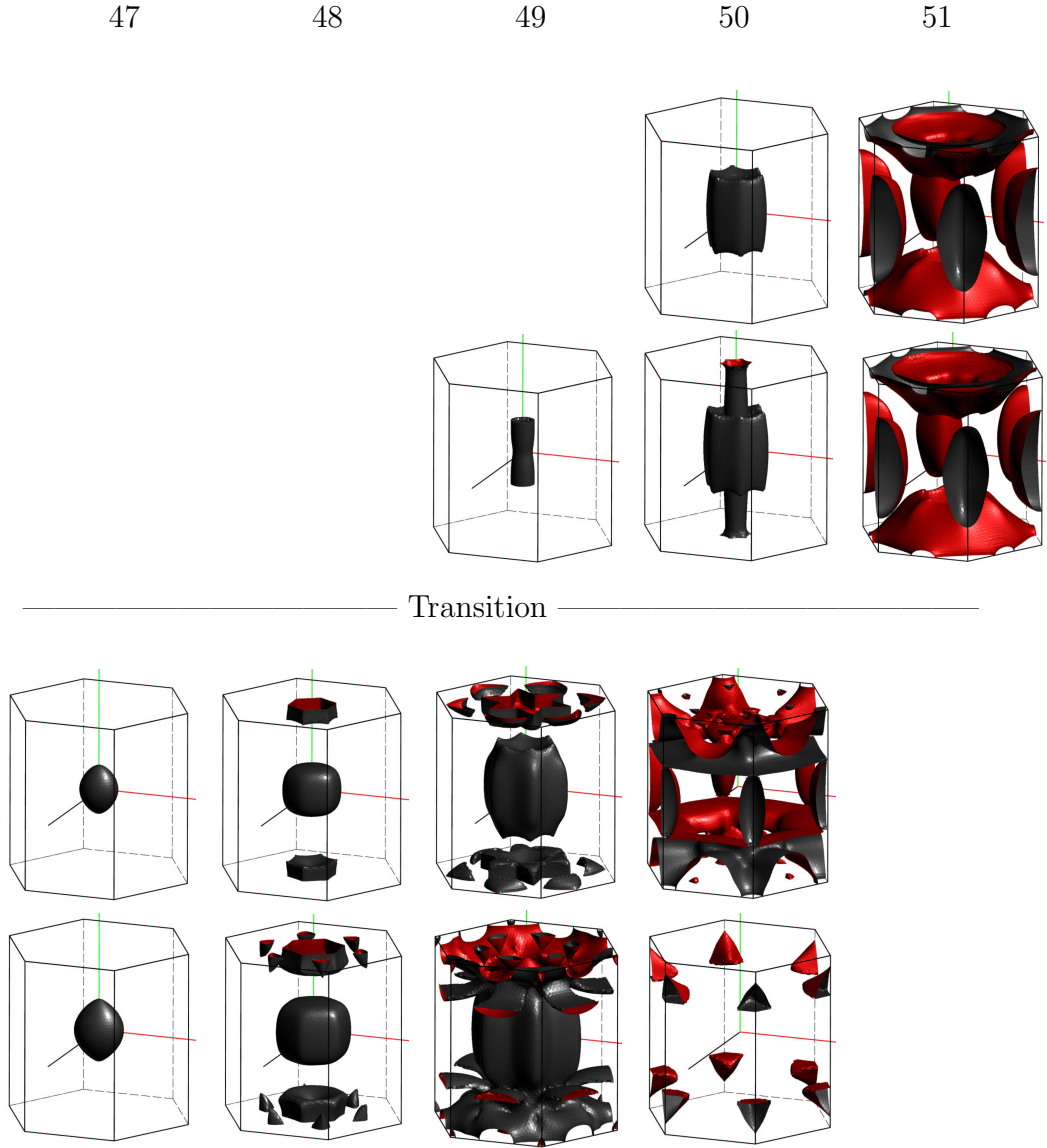


Figure 3.14: Spin-up part of the Fermi surface of YCo_5 . First row: $V = 76.16 \text{ \AA}^3$. Second row: $V = 73.83 \text{ \AA}^3$. Third row: $V = 72.53 \text{ \AA}^3$. Last row: $V = 67.47 \text{ \AA}^3$. All sheets of the Fermi surface, which are plotted in the same column belong to the same band. The corresponding number of the band is written at the top of each column.

transition exhibit a totally new appearance.

Figures 3.15 and 3.16 show the spin-down part of the Fermi surface. Here again are minor topological changes of the Fermi surface within the HS or the LS phase. Within the HS phase a neck breaks in band number 43. In band number 44, there are tiny hole surfaces disappearing and necks are created at the top of the BZ. Though it cannot be easily seen in the perspective view of this figure, there are some necks created in band number 45, which can be seen in a top view of this Fermi surface sheet. Band number 46 (Figure 3.16) does not exhibit any Lifshitz transitions within the HS phase. At volumes slightly larger than the transition volume a new sheet of Fermi surface appears.

Going back to Figure 3.15, in the LS phase, two bands (number 43 and 44), which intersect the Fermi energy only with one respective two maxima do not intersect the Fermi level at higher pressures any more. In the Fermi surface sheet number 45 some necks break and some pockets disappear in the LS phase under growing pressure. Turning to the first column of Figure 3.16 (band number 46) a lot of topological changes take place within the LS phase. In the LS state of band number 47 a neck breaks and new pockets of the Fermi surface appear. Under high pressure band number 48, which has no intersections with the Fermi level even at smaller volumes than the transition volume, crosses the Fermi energy making electron pockets.

If one compares the spin-down part of the Fermi surface for larger and smaller volumes than the transition volume, one may think, that an error occurred by choosing the right column for the picture because the Fermi surface sheets in the HS state show much similarity with the column one further on the right of the LS state Fermi surface plots. But this is not the case! Indeed a thorough investigation of the band structure reveals, that a sudden big shift of the bands take place at the transition. The spin-up bands move higher in energy relative to the Fermi level with increasing pressure and the spin-down bands move downwards in energy with respect to the Fermi level and increasing pressure. This large shift of the bands gives rise to a whole new appearance of the Fermi surface after the transition took place.

3.1.11 *Conclusions*

We found, that YCo_5 undergoes a first order Lifshitz transition under pressure. The transition takes place, when the volume of the unit-cell shrinks down to $V \approx 73.8 \text{ \AA}^3$. At the transition the spin-up bands are shifted to

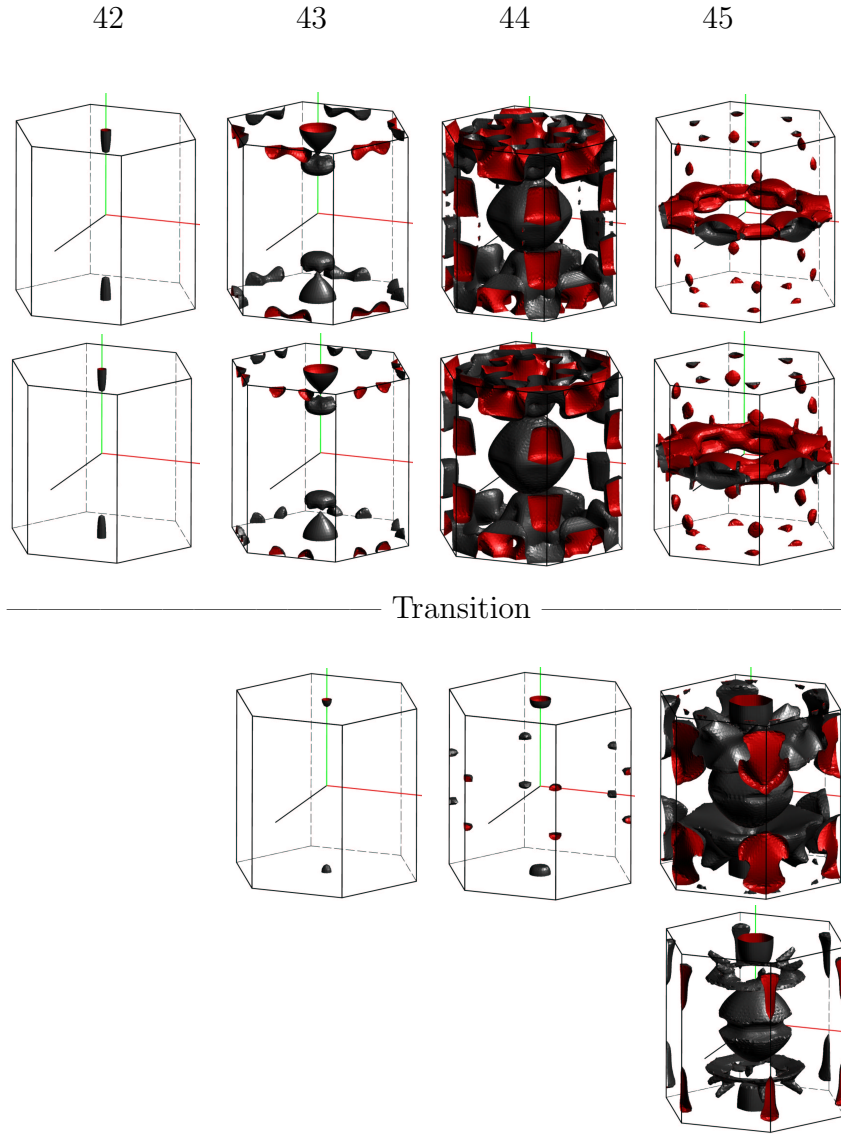


Figure 3.15: Fermi surface plots of the first four bands of the spin-down part of the Fermi surface of YCo_5 . First row: $V = 76.16 \text{ \AA}^3$. Second row: $V = 73.83 \text{ \AA}^3$. Third row: $V = 72.53 \text{ \AA}^3$. Last row: $V = 67.47 \text{ \AA}^3$. All sheets of the Fermi surface, which are plotted in the same column belong to the same band. The corresponding number of the band is written at the top of each column.

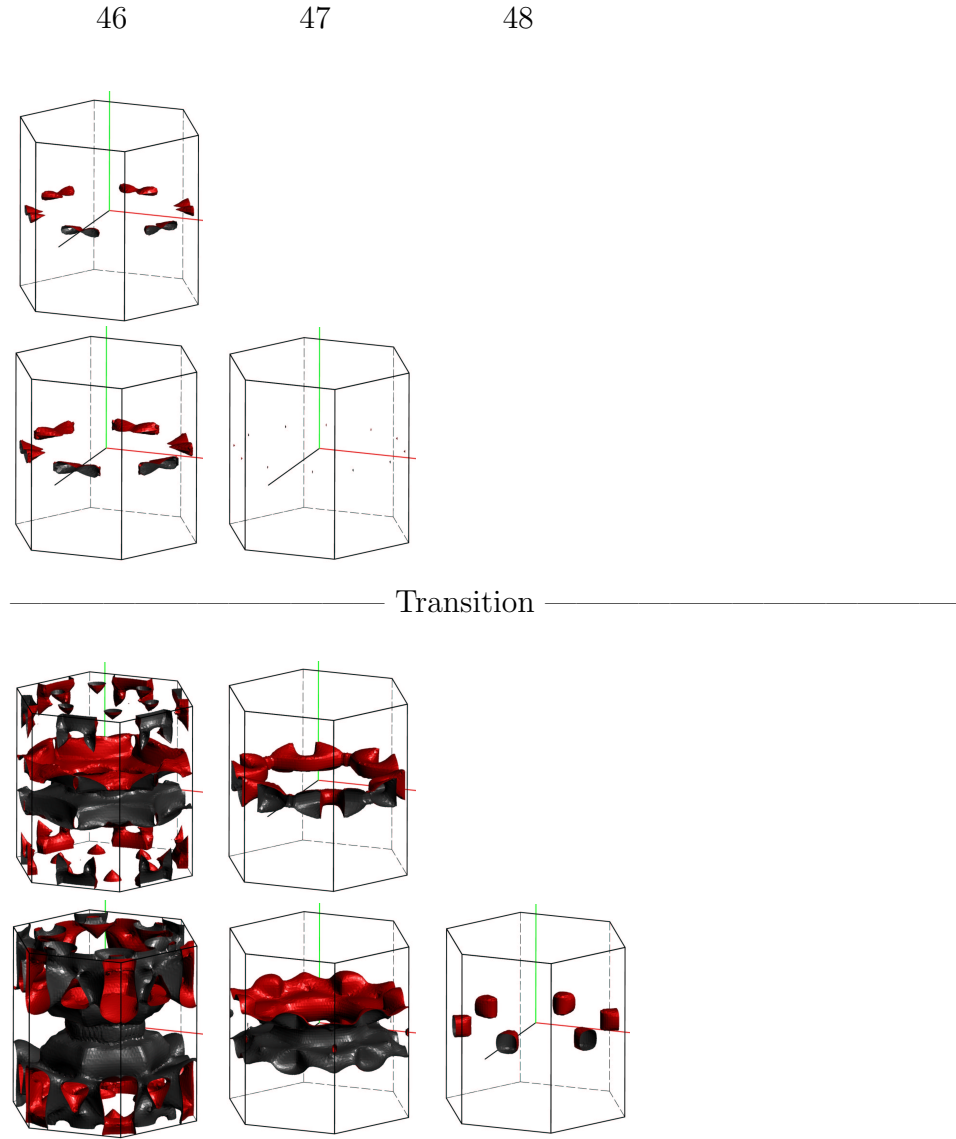


Figure 3.16: Fermi surface plots of the last three bands of the spin-down part of the Fermi surface of YCo_5 . First row: $V = 76.16 \text{ \AA}^3$. Second row: $V = 73.83 \text{ \AA}^3$. Third row: $V = 72.53 \text{ \AA}^3$. Last row: $V = 67.47 \text{ \AA}^3$. All sheets of the Fermi surface, which are plotted in the same column belong to the same band. The corresponding number of the band is written at the top of each column.

higher energies and the spin-down bands are shifted towards lower energies. This shift results in a totally new appearance of the Fermi surface. Furthermore it reduces the total magnetic moment from $6.3 \mu_B/\text{cell}$ to $4.1 \mu_B/\text{cell}$. Due to the broadening of the bands under pressure the upper edge of the Co $3d$ band crosses the Fermi level at the transition, so that the transition can as well be considered as a transition from strong to weak ferromagnetism. The crystal symmetry is preserved through the transition but the c -axis collapses at the transition, which results in a volume collapse of about 1.4%.

Thus YCo_5 undergoes an isomorphic volume collapse under pressure.

3.2 PREDICTIONS FOR LaCo_5 UNDER PRESSURE

A substance very similar to YCo_5 is LaCo_5 . Both crystallize in the same structure (P6/mmm, space group 191, compare Figure 3.1). The only difference is, that La atoms are bigger than Y atoms, because La is in the next period of the periodic table. Therefore the zero pressure lattice parameters of LaCo_5 are different to those of YCo_5 , in particular the unit cell of LaCo_5 is larger than the unit cell for YCo_5 . Measurements determined the lattice parameters of LaCo_5 to $a = 5.105 \text{ \AA}$ and $c = 3.966 \text{ \AA}$ [34]. Motivated by the results of YCo_5 we were curious to find an analogous transition in LaCo_5 and so we applied the same calculations, which were done for YCo_5 in the previous Section, to LaCo_5 .

This chapter is constructed like follows: Section 3.2.1 contains details of the calculations. Some remarks about the convergence of parameters with special emphasis to differences between different basis sets are made in Section 3.2.2, while Section 3.2.3 comprises the results about the magnetic moment in LaCo_5 under pressure. In Section 3.2.4 the lattice parameters and the development of the unit cell volume under pressure are studied and Section 3.2.5 shows band structure and DOS of LaCo_5 . Finally Section 3.2.6 concludes the chapter.

3.2.1 Method of calculation

The calculations were performed with FPLO [4], release 3. The La basis included $1s2s2p3s3p3d4s4p4d$ as core states, $5s5p$ as semi-core, $6s6p5d$ as valence and the $4f$ state as a polarization state. The Co basis included $1s2s2p$ as core states, $3s3p$ as semi-core states, $4s4p3d$ as valence and $4d4f$

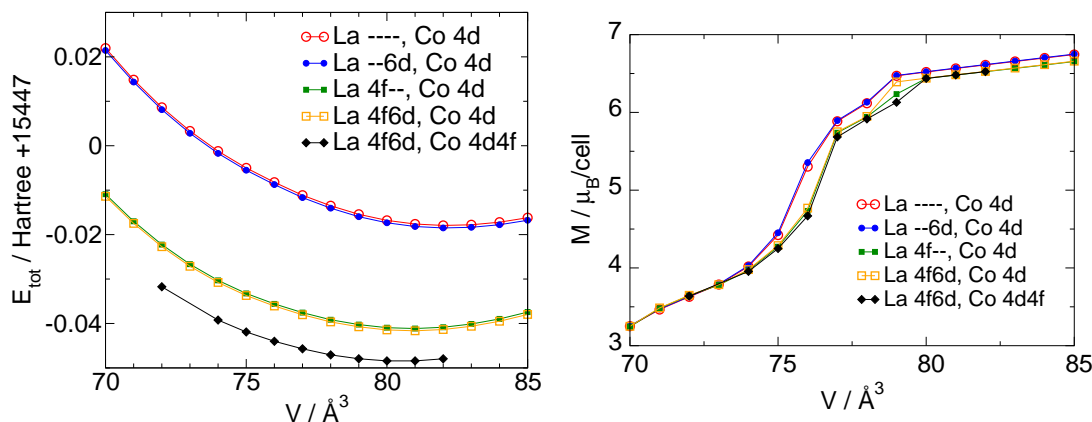


Figure 3.17: Total energy (left panel) and magnetic moment (right panel) versus volume for different bases. Core, semi-core and valence states are the same in all curves. Only polarization states differ. Which states are used as polarization states is written in the legends. Polarization states have $x_0 = 0.9$.

as polarization states. A \mathbf{k} -mesh subdivision of $36 \times 36 \times 36$ was used, which corresponds to 2413 \mathbf{k} -points in the irreducible part of the BZ. We used 2000 Fourier components of the Ewald-potential. All calculations have been done scalar relativistic. For the exchange-correlation potential we used LSDA in the version of Perdew Wang 92 [30].

3.2.2 Convergence of parameters

To find the "best choice" of input-parameters, convergence tests were done with different bases, different \mathbf{k} -points and various numbers of Fourier components of the Ewald-potential in analogy to YCo_5 (compare Section 3.1.3).

Figure 3.17 shows total energies (left panel) and the magnetic moment (right panel) in dependence of the unit cell volume for different bases. The core, semi-core and valence states are the same in all bases, only the polarization states differ as indicated in the legends.

Let's concentrate on the left panel. One can see that the total energy hardly depends on the La 6d states. Inclusion of La 6d states lowers the total energy negligibly. But it makes a difference if the basis includes the La 4f states. If they are included, the total energy is considerably lowered

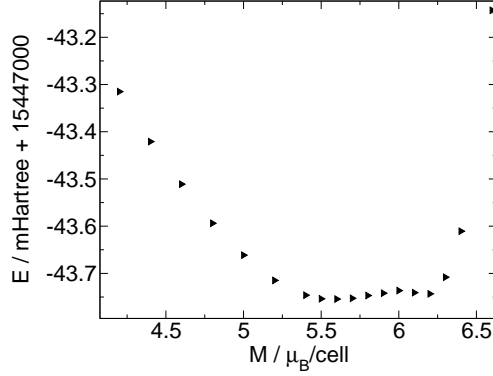


Figure 3.18: FSM calculation for $V = 76.0 \text{ \AA}^3$ and $c/a = 0.81$.

(about 20 mHartree). With La 4*f* states the zero pressure volume is 1 \AA^3 smaller than without La 4*f*, which means that the La 4*f* states contribute substantially to binding. Inclusion of the Co 4*f* state causes a further lowering of the total energy and shifts the minimum to even smaller volumes ($V_0 = 80.5 \text{ \AA}^3$ instead of $V_0 = 80.9 \text{ \AA}^3$).

Now focus on the right panel. Here the volume dependence of the magnetic moment for different bases is shown. It can be seen, that the magnetic moment depends only for $V > 73 \text{ \AA}^3$ on the basis. Inclusion of the La 4*f* state makes the magnetic moment smaller.

For the calculations we used the La 4*f* states and the Co 4*d* and 4*f* states since inclusion of the 4*f* states of both atoms lowers the total energy considerably. We did not include the La 6*d* states in the basis, since their impact is negligible.

3.2.3 The magnetic moment of LaCo_5 under pressure

For we expected LaCo_5 to show a transition like in YCo_5 , FSM calculations were done in the expected transition region. The results exhibit a double-well structure of $E(M; (c/a)_j, V_j)$ for most values of $(c/a)_j$ and V_j , showing a stable and a meta-stable state. Figure 3.18 shows an example, where $V_j = 76.0 \text{ \AA}^3$ and $(c/a)_j = 0.81$.

In Figure 3.19 the magnetic moment against volume is displayed. Note the similarity to YCo_5 (compare Figure 3.4)! Even the magnetic moment in the HS state has about the same value, which is already known from

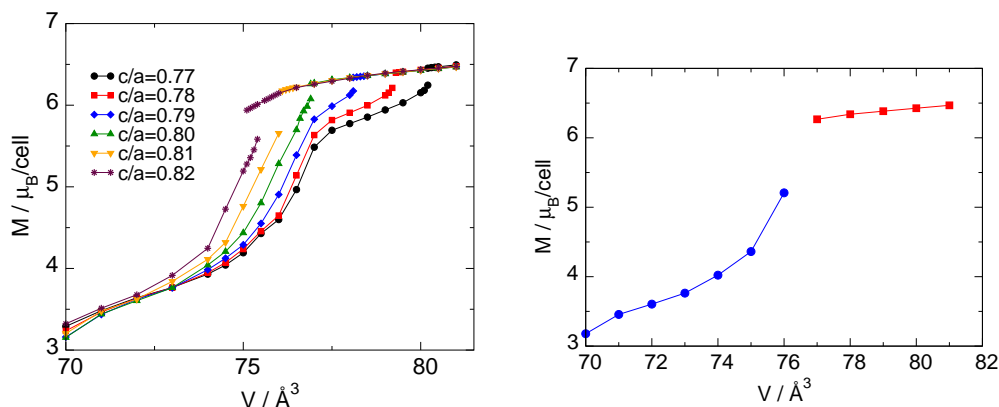


Figure 3.19: Left panel: Magnetic moment in dependence of the volume for various fixed c/a . Right panel: Magnetic moment against volume for relaxed c/a . The blue dots (red squares) are LS (HS) values.

experiment [34].

The left panel of Figure 3.19 shows results for various fixed c/a ratios. It can be seen that in the HS state the magnetic moment does not depend on the c/a ratio. But the volume at which the LS branch starts depends strongly on the c/a ratio. The larger the c/a ratio the smaller the unit cell volume where the LS branch starts. Like in YCo_5 the dependence of the magnetic moment on volume shows additional features for small c/a .

The right panel displays the magnetic moment against volume for relaxed c/a . The blue dots (red squares) are LS (HS) values. It is obvious that in the HS phase the magnetic moment is saturated, it is nearly constant, only a very small decrease with decreasing volume is seen. For the pressure range up to 1 GPa this was as well observed in experiment [35]. At $V = 77 \text{ \AA}^3$ the transition takes place. Thus, LaCo_5 has not only a bigger zero pressure volume than YCo_5 , but also the transition takes place at larger volumes (YCo_5 : $V = 73.8 \text{ \AA}^3 \rightarrow V = 72.8 \text{ \AA}^3$). In the LS phase the magnetic moment is decreasing rapidly. The steep decrease seems to be less pronounced than in YCo_5 but this may be due to the fact that for LaCo_5 we have not so many points calculated in the transition region. (If one looks at the left panel, the region of steep decrease can be clearly distinguished from the region of slow decrease.)

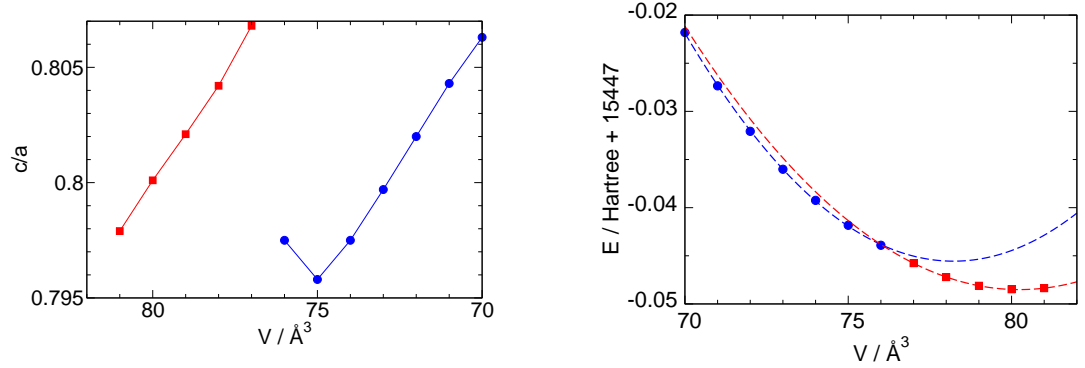


Figure 3.20: Left panel: Relaxed c/a ratio against volume. Note that the scale of the horizontal axis is inverted, so that pressure increases from left to right. Right panel: Total energy versus volume. The dashed lines are parabolas fitted to the data. Red squares (blue circles) are HS (LS) data.

3.2.4 Lattice geometry and elastic anomaly under pressure

Since LaCo_5 is hexagonal like YCo_5 , we have to find out, how the c/a ratio changes under hydrostatic pressure. This is done like in Section 2.2.1 derived: To each volume the c/a ratio, which is lowest in energy is assigned. The result can be seen in the left panel of Figure 3.20. Here the volume-dependence of the relaxed c/a ratio is shown. Note, that the volume increases from right to left, so if one reads the figure from left to right, the behavior of c/a with increasing pressure can be seen. Again note the similarity to YCo_5 (Figure 3.6). Starting at ambient conditions and then increasing the pressure, the c/a ratio increases linearly with decreasing volume. At a unit cell volume of about 77\AA^3 the transition takes place. The volume collapses to 76\AA^3 and the c/a ratio jumps from $c/a = 0.807$ to $c/a = 0.797$. It decreases further until the volume reaches $V = 75 \text{\AA}^3$ and then the c/a starts again to increase linearly with decreasing volume.

The right panel of Figure 3.20 shows total energies against volume. The blue dots (red squares) are LS (HS) values. To each of the phases there is a parabola fitted (dashed line). It is obvious that for low pressures (large volumes) the HS state is energetically much more favorable. At $V = 76 \text{\AA}^3$ this changes and the LS state becomes lower in energy. If one constructs a common tangent to both parabolas, the points, where the HS and the LS

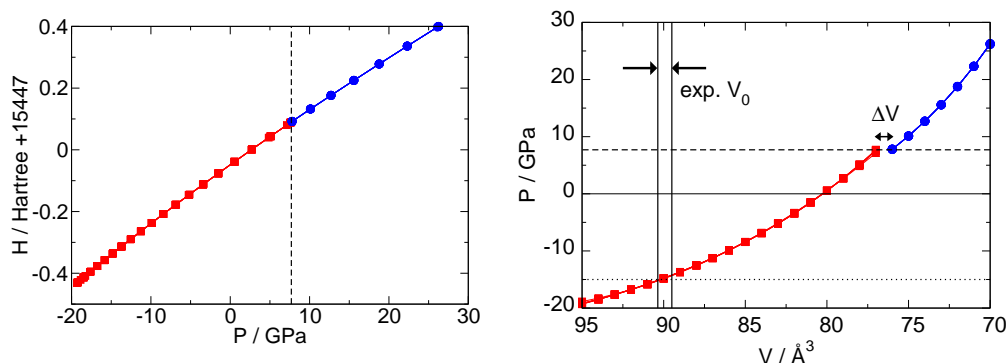


Figure 3.21: Left panel: Enthalpy versus pressure. The dashed line marks the transition pressure. Right panel: Hydrostatic pressure against unit cell volume. Note the inversed scale of the volume-axis! The dotted line marks the experimental zero pressure. The dashed line marks the transition pressure. The two vertical lines denote two different measured zero pressure volumes [28, 34]. Blue dots (red squares) denote LS (HS) values.

parabola touches the tangent denote these two points between which the transition and the volume collapse take place. Such a common tangent construction is equal to the calculation of the enthalpy, which is shown in Figure 3.21, left panel. The point (P_c, H_c) , where the two branches cross, determine the transition pressure $P_c = 7.7$ GPa of a first order phase transition.

The equation of state is displayed in the right panel of Figure 3.21. The similarity to YCo_5 (compare Figure 3.9) is obvious. Here again blue dots (red squares) denote LS (HS) values. Please note the inversed scale of the volume-axis! With increasing pressure the volume decreases. At the transition ($P = 7.7$ GPa, dashed line) the volume collapses. From the experience with YCo_5 we know, that the transition takes place at a much higher pressure than theory yields. Nevertheless one can correct for this if one takes the pressure-distance between the experimentally observed ground state volume and the calculated transition-pressure instead of the smaller ground state volume LDA gives. In the case of YCo_5 after this change the transition-pressure is in perfect agreement with observation [7]. For LaCo_5 LDA yields a ground state volume of $V_0^{\text{LDA}} = 80 \text{ \AA}^3$. If the pressure-axis is shifted that way, that the experimentally observed ground state volume $V_0^{\text{exp}} \approx 90 \text{ \AA}^3$ corresponds to zero pressure (dotted line), it must be shifted by 15 GPa. *Thus I can*

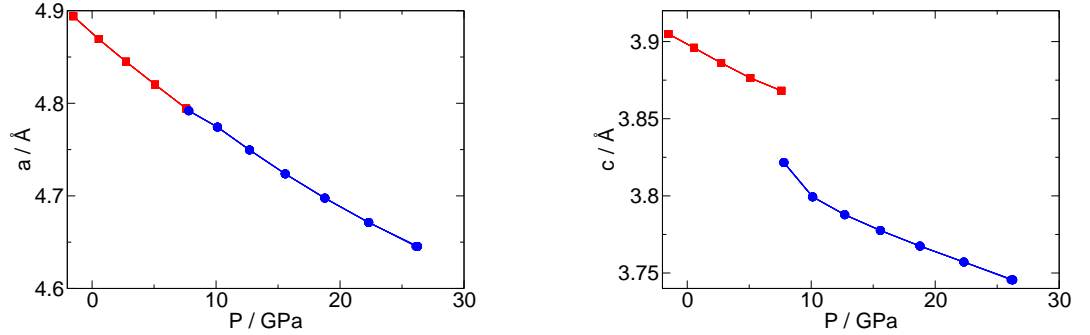


Figure 3.22: a -axis (left panel) and c -axis (right panel) versus pressure. Blue circles (red squares) denote LS (HS) data.

predict, that if one measures the lattice geometry of LaCo_5 under hydrostatic pressure, one should find a volume collapse around a pressure of 23 GPa.

Figure 3.22 shows the contraction of the lattice constants with pressure. Red squares (blue circles) correspond to HS (LS) data. The lattice constant in the hexagonal plane, denoted by a , is more or less smoothly decreasing with pressure — even through the transition, whereas the lattice constant c shows a jump at the transition. This jump induces the volume collapse and the jump of the c/a ratio.

3.2.5 Band structure and DOS of LaCo_5

The band structure of LaCo_5 is plotted in Figure 3.23. The upper panel shows the band structure at zero pressure and the lower panel displays the band structure for $V = 76.0 \text{ \AA}^3$, a volume slightly smaller than the transition volume. The band structure of LaCo_5 resembles the band structure of YCo_5 (compare Figure 3.12). The flat band in the hexagonal plane (Γ -M-K- Γ), that we have already found in YCo_5 , is present in LaCo_5 as well.

Figure 3.24 shows the total DOS of LaCo_5 . The strong peak in the spin-up DOS close to the Fermi level, which results from the flat band in the hexagonal plane, is clearly seen. It is the upper edge of the Co $3d$ band. Like in YCo_5 , the Co $3d$ band is fully populated in the HS state, whereas it gets partially depopulated in the LS state since at the transition this peak crosses the Fermi energy.

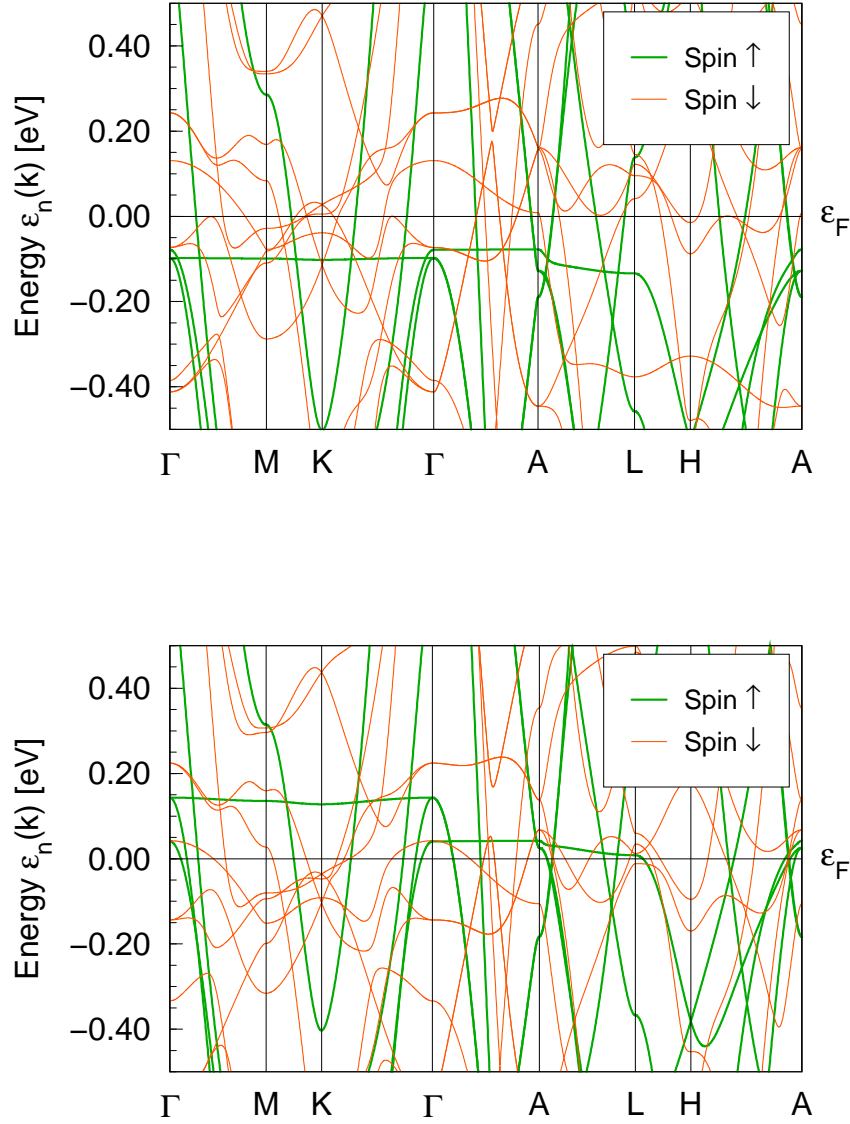


Figure 3.23: Upper panel: band structure of LaCo_5 around the Fermi energy at zero pressure. Lower panel: band structure of LaCo_5 around the Fermi energy for $V = 76.0 \text{ \AA}^3$, $c/a = 0.7975$. One can see that the flat band in the hexagonal plane (Γ -M-K- Γ) is below the Fermi level at zero pressure and above it for pressures higher than the transition pressure.

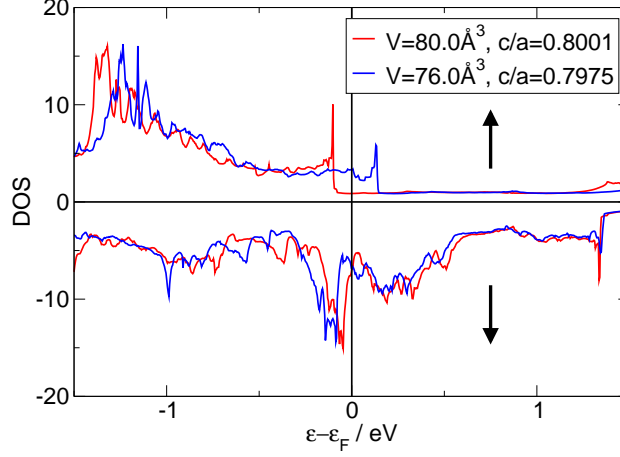


Figure 3.24: Total DOS plotted for both spin channels. The red curve belongs to LaCo_5 in the HS state and the blue curve shows the total DOS in the LS state.

3.2.6 Conclusions

We found that in LaCo_5 a similar first order transition takes place like in YCo_5 . The transition happens at a pressure of 23 GPa when the volume of the unit cell has reached $V = 77 \text{ Å}^3$. There the c lattice constant collapses and induces a volume-collapse. The peak, which results from a flat band in the hexagonal plane and which is situated at the upper $3d$ band edge, crosses the Fermi level at the transition and the magnetic moment decreases.

3.3 LIFSHITZ TRANSITIONS IN OS UNDER PRESSURE

The search for Lifshitz transitions [5] is a renewed subject of interest. As an example for a recent work, in 1998 Godwal *et al.* [36] found a Lifshitz transition in AuIn_2 , where measurements yield an anomaly in the electrical resistivity and in the thermoelectric power in the 2 – 4 GPa pressure range, but angle-dispersive x-ray-diffraction measurements do not yield a structural change. LMTO-ASA calculations revealed that there a Lifshitz transition

is taking place because at the Γ -point a maximum in the band structure is crossing the Fermi level [36]. The similar compound AuAl_2 does not show a Lifshitz transition [37]. Sin'ko and Smirnov calculated the Fermi surface of ferromagnetic α -Fe in the range $0.86 \leq V/V_0 \leq 1.23$ and found twelve electronic topological transitions [38]. A big controversial discussion is going on in the literature, if Zinc shows an anomaly in c/a due to Lifshitz transitions (see Ref. [39] and references therein). Up to now it seems to be clear that Zn indeed exhibits Lifshitz transitions under pressure [40–43] but if there is an anomaly in c/a connected to these transitions remains unclear. Very accurate experiments could not detect any anomalies being larger in size than the experimental error [44, 45].

Osmium was measured by Occelli *et al.* [8] under pressure with neon (low pressure regime) and helium (high pressure regime) as pressure transmitting media and an exposure time of about 4 seconds. They found an anomaly in the c/a ratio under applied pressure and claimed that this could be an evidence for a Lifshitz transition. Takemura [9] did measurements in the same pressure range with neon as a pressure transmitting medium but with an exposure time of 2 minutes. He did not find any anomaly in his data. To explore the hypothesis of Occelli *et al.* [8] from the theoretical side, we did very accurate first principle calculations applying the DFT-based band structure code FPLO [4].

Osmium has a hexagonal close packed structure (hcp, $P6_3/mmc$, Space group 194) with two atoms in the unit cell. It belongs to the 5d transition metals and is one of the densest elements. It has the largest bulk modulus of all metals and since a few years there is a discussion in the literature, if its bulk modulus is even larger than diamond [8, 9, 46–49].

This chapter is constructed like follows: Section 3.3.1 contains details of the calculation. Results of total energy calculations are shown in Section 3.3.2, while in Section 3.3.3 the Fermi surface of Osmium under pressure is studied in detail. Section 3.3.4 contains the band structure and Section 3.3.5 the DOS of Osmium. In Section 3.3.6 the development of the lattice parameters under pressure is studied and our results are compared to measurements and earlier calculations. Section 3.3.7 explores the quality of different fits to the development of c/a under pressure. The chapter is concluded in Section 3.3.8 and Section 3.3.9 comprises like an appendix the parameters used for fitting.

3.3.1 Method of calculation

The calculations were performed in a four-component full relativistic way with FPLO [4], release 5. After test calculations with different bases we decided to use a minimum basis consisting of $4f5s5p$ states in the semicore and $6s6p5d$ states in the valence. All lower lying states were put in the core. A k -mesh subdivision of $48 \times 48 \times 48$ k -points in the full BZ was used, which corresponds to 5425 k -points in the irreducible part of the BZ. For calculating the DOS, the k -mesh was enhanced to $96 \times 96 \times 96$ k -points in the full BZ (40033 k -points in the irreducible BZ), which is still not enough to resolve the small anomalies of the DOS due to the Lifshitz transition but it is at the limits of available computer memory. For the exchange-correlation potential we used LDA in the version of Perdew Wang 92 [30].

3.3.2 Total energy calculations

Figure 3.25 shows the total energy of Osmium plotted against volume for zero temperature, where the c/a ratio has been relaxed for each volume. The dashed line shows the experimental volume (taken from Ref. [8]), determined in a room temperature experiment. The calculated zero pressure and zero temperature volume is 0.3% smaller than the measured room-temperature volume. Accounting for thermal expansion, provides an almost perfect agreement. In fact this is a known but not yet understood feature of LDA, that it reproduces the ground state volume for the heavy 5d elements [10].

The inset of Figure 3.25 proves the high accuracy of the calculations, because FPLO [4] yields a very smooth energy-curve, even in the μ Hartree range.

3.3.3 The Fermi surface of Osmium under pressure

The Fermi surface of Osmium has been calculated for different c/a ratios and various unit cell volumes in the range $22.0 \text{ \AA}^3 \leq V \leq 28.0 \text{ \AA}^3$. It consists of four sheets (see Figure 3.27). At zero pressure the first sheet (left panel) consists of hole ellipsoids located at the line between L and M (for the location of the symmetry points in the BZ see Figure 3.26). In the publication of Occelli *et al.* [8] it was suggested that these hole ellipsoids should vanish under pressure. The second sheet (second panel from the left) contains a big surface usually called "monster", which is closed in z -direction but open orbits are

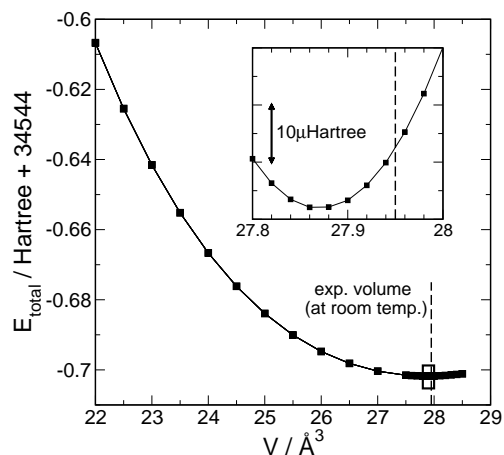


Figure 3.25: Total energy versus unit cell volume with relaxed c/a ratio at zero temperature. The dashed line marks the experimental room-temperature volume [8]. Inset: magnification of the total energy versus volume curve around the minimum. In the large graph this region is marked with a box.

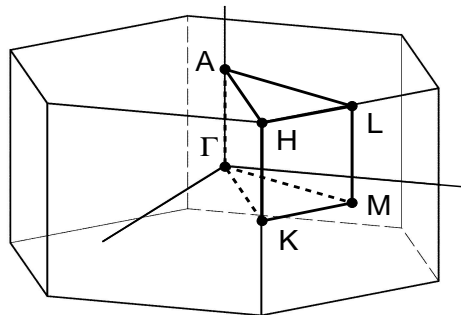


Figure 3.26: Symmetry points in the hexagonal BZ.

present in the hexagonal plane. The third and fourth sheet are closed Fermi surface sheets, which are nested and centered around the Γ -point. The inner one of the two is waisted. Our calculated Fermi surface of the ground state agrees well with de Haas-van Alphen measurements of Kamm and Anderson [50] and with the calculated Fermi surfaces of Smelyansky *et al.* [51] and Ma *et al.* [52]

In Figure 3.28 the Fermi surface at zero pressure (first row, $V = 27.87 \text{ \AA}^3$, $c/a = 1.585$) is compared to the Fermi surface calculated at a very high pressure of about 180 GPa (second row, $V = 22.0 \text{ \AA}^3$, $c/a = 1.5968$). It is obvious, that the hole ellipsoid between L and M, displayed in the first column of Figure 3.28, where Occelli *et al.* [8] claimed that it may vanish under pressure, does not disappear. On the contrary, it grows. Nevertheless there is a Lifshitz transition in the first sheet of the Fermi surface: at the L-point a small hole ellipsoid appears under pressure. The second and third

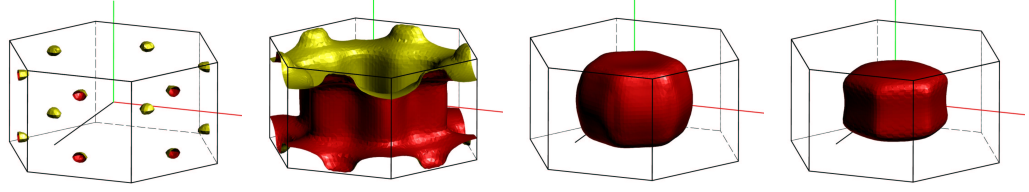


Figure 3.27: The Fermi surface of Osmium at zero pressure. Red and yellow colors denote electron and hole surfaces, respectively.

column of Figure 3.28 display the second sheet of the Fermi surface in a side view (second column) and in a top view (third column), respectively. In the picture showing the side view, the BZ is shifted such that its edge lies in the center of the image. In these two views it is much easier seen than in the second panel of Figure 3.27 that this part of the Fermi surface is closed in z -direction, since in this direction there is no connection between this Fermi surface sheet and its image in the neighboring BZ (first row, second panel). But if we have a look at the corresponding pictures, which show the second Fermi surface sheet under pressure, we observe another Lifshitz transition: a neck is created, centered close to L at the line between L and H. Thus this sheet of Fermi surface becomes open in z -direction. The third and the fourth sheet of the Fermi surface are not displayed in Figure 3.28 because the third Fermi surface sheet does not change under pressure and the fourth Fermi surface sheet looks from outside like at zero pressure. The last column of Figure 3.28 shows cuts through the fourth part of the Fermi surface. Here, a third Lifshitz transition happens under pressure, hidden inside the fourth sheet of the Fermi surface: at zero pressure the fourth sheet of Fermi surface is empty inside but under pressure a hole ellipsoid appears at the Γ -point.

Thus three Lifshitz transitions take place in Osmium under pressure:

- A hole ellipsoid appears in the first Fermi surface sheet at the L-point.
- In the second sheet a neck is formed close to L at the line between L and H.
- An additional hole ellipsoid centered at Γ appears inside the fourth Fermi surface sheet.

Furthermore our calculations show, that all three Lifshitz transitions do not happen all at the same lattice constants. But there is one peculiarity

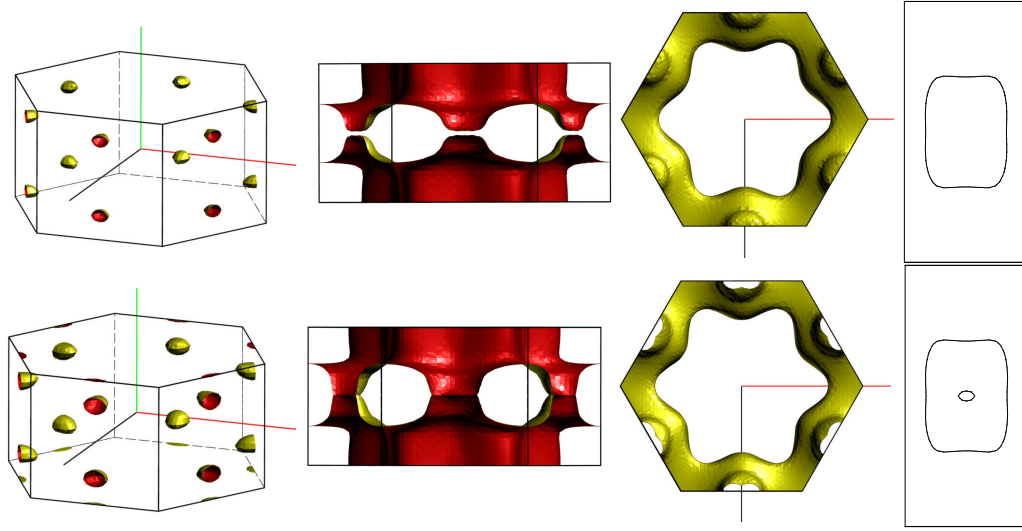


Figure 3.28: Comparison between the Fermi surface of Osmium at zero pressure ($V = 27.87 \text{ \AA}^3$ first row) and under high pressure (second row, $P \approx 180 \text{ GPa}$, $V = 22.00 \text{ \AA}^3$) The first column shows the first sheet of the Fermi surface, the second and the third columns show the second sheet of the Fermi surface in a side view and in a top view, respectively. In order to make the connectivity better visible, the side-view is shifted in z -direction, such that the BZ edge lies in the middle of the picture. The fourth column displays a cut through the fourth sheet of the Fermi surface in the yz -plane. Colors are explained in Figure 3.27

with the neck and the ellipsoid at the L-point. If one compares the third panel in the second row of Figure 3.28 with Figure 3.29, it is obvious that the topology of this sheet of Fermi surface differs in the two figures though in both cases the neck exists. Considering the line H-L-H in the BZ, there are two necks for the larger volume (Figure 3.29), which melt under pressure into one neck (third panel in the second row of Figure 3.28). Exactly, when the two necks touch and melt into one, the ellipsoid appears at the L-point. As a consequence the ellipsoid has the same extent in direction L-A than the neck is extended in this direction. This can be seen from the band structure (compare Section 3.3.4) since the band responsible for the neck and the band responsible for the ellipsoid at the L-point are degenerate in direction L-A.

When calculating the Fermi surface for different unit cell volumes and c/a ratios, one observes for each Lifshitz transition a line in the c/a - V -plane

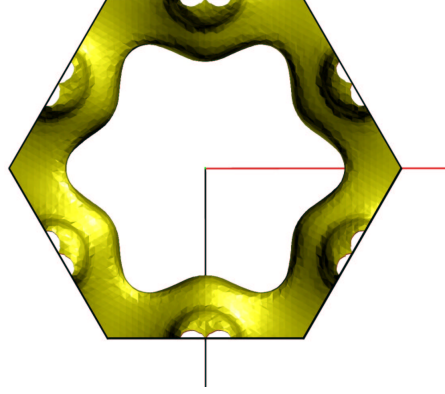


Figure 3.29: Second sheet of the Fermi surface at $V = 23.2 \text{ \AA}^3$, $c/a = 1.595$

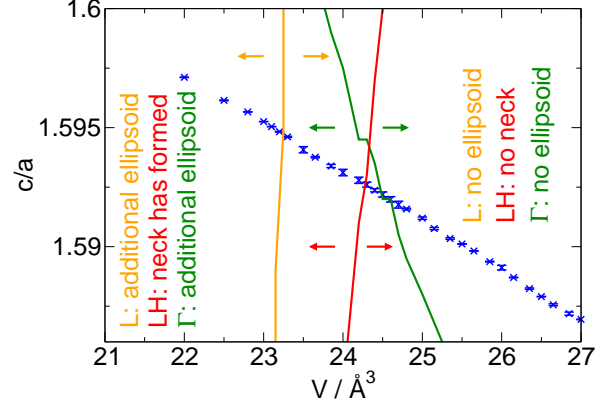


Figure 3.30: Dependence of the ETT on volume and c/a . Blue symbols with error bars: calculated relaxed c/a versus unit cell volume. Green line: ETT at the Γ -point. Red line: ETT at the symmetry-line LH. Yellow line: ETT at the L-point.

(see Figure 3.30), where on one side of the line an additional ellipsoid or a neck is created and on the other side of the line there is no neck or no additional ellipsoid. In the case of the Lifshitz transition at the Γ -point for decreasing volume the c/a ratio increases at which the transition takes place (green line in Figure 3.30). The kinks in the line are due to the coarse grid of the $(V, c/a)$ -mesh at which the Fermi surface has been calculated. For the creation or disruption of the neck at the symmetry line LH it is the other way round: with decreasing volume the c/a ratio decreases at which the transition takes place (red line in Figure 3.30). The critical volume for the transition at the L-point (yellow line in Figure 3.30) has only a very weak dependence on c/a . For c/a ratios in the range $1.58 \leq c/a \leq 1.60$ the additional ellipsoid is formed at a unit cell volume of approximately 23.2 \AA^3 . The FPLO-results for the c/a ratio versus volume under hydrostatic pressure are also displayed in Figure 3.30 (blue symbols). With this information one can read from this figure that under hydrostatic pressure at first the additional ellipsoid at the Γ -point appears ($V = 24.60 \text{ \AA}^3$), if pressure is further increased, then the neck is formed ($V = 24.20 \text{ \AA}^3$) and at much higher pressures finally the additional

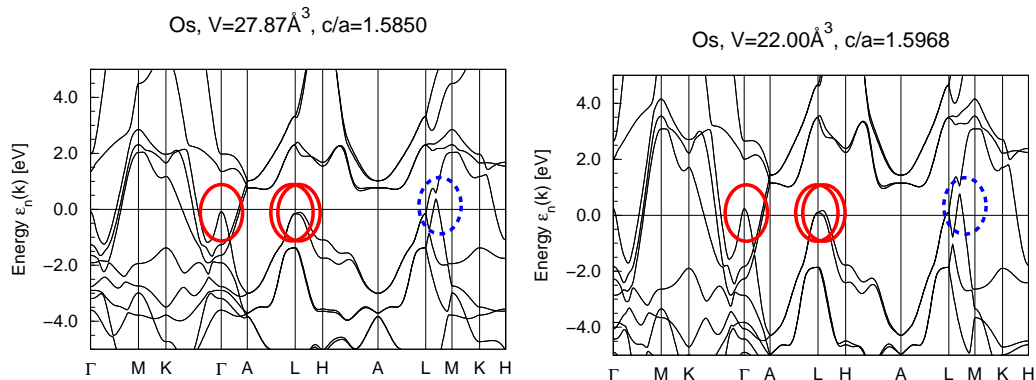


Figure 3.31: Band structure of Osmium. Left panel: zero pressure. Right panel: $P \approx 180$ GPa. The red circles (full lines) mark points in \mathbf{k} -space where a band maximum crosses the Fermi level under pressure. The blue circle (dashed line) marks the location where a maximum crossing the Fermi energy is proposed by Occelli *et al.* [8] but disproved by our calculations.

ellipsoid at the L-point appears ($V = 23.20 \text{ Å}^3$). For the corresponding pressures to these volumes see Figure 3.34.

3.3.4 Band structure of Osmium under pressure

The topological changes of the Fermi surface should be visible in the band structure of Osmium as well. For each appearing hole ellipsoid (and in Osmium all appearing/disappearing ellipsoids in the Fermi surface are of hole type in the considered volume range) a maximum in the band structure should cross the Fermi energy under pressure at that symmetry point of the BZ, where the additional ellipsoid appears. In the case of a neck a saddle-point should cross the Fermi level, which may either look like a maximum or minimum in the band structure, depending on the direction of the projection.

Figure 3.31 shows the band structure of Osmium for zero pressure (left panel) and under a high hydrostatic pressure of about 180 GPa (right panel). It is obvious that the band structure contains several maxima and minima. The result of the previous section was, that Osmium exhibits three Lifshitz transitions in the considered pressure range (compare Section 3.3.3). These are located at the Γ -point, the symmetry line between L and H and at the L-point. If we now draw our attention to the mentioned points in Figure 3.31, we observe, that the band structure indeed exhibits maxima there, marked

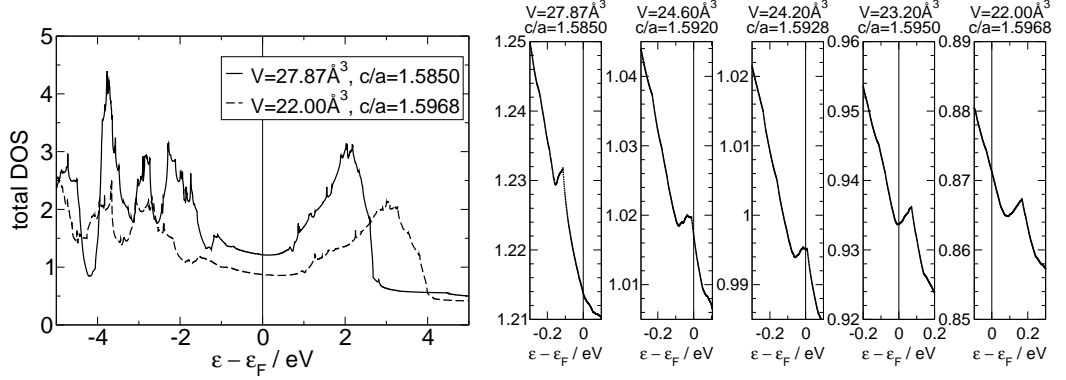


Figure 3.32: Left panel: Total DOS of Osmium at two different volumes. Full lines: zero pressure; dashed lines: $P \approx 180$ GPa. Five panels on the right: magnification of the DOS around the Fermi level at zero pressure, at that pressure, where the ellipsoid at the Γ -point appears, at that pressure, where the neck is created, at that pressure, where the ellipsoid at the L-point appears and at a pressure of about 180 GPa (from left to right).

with a red circle. By comparing the red encircled maxima in both panels, one finds out, that all three lie below the Fermi level at zero pressure but are above the Fermi energy at high pressures.

The blue circle in Figure 3.31 marks the place where a maximum crossing the Fermi energy is proposed by Occelli *et al.* [8]. But by comparing both panels of Figure 3.31 it is obvious that this maximum does not fall below the Fermi level under pressure and thus there is no Lifshitz transition on the line between L and M in the hydrostatic pressure range $0 \leq P \leq 180$ GPa.

3.3.5 DOS of Osmium

In Figure 3.32 the total DOS for Osmium is shown in the left panel. The full line denotes zero pressure and the dashed line corresponds to a high pressure of about 180 GPa. The DOS in the energy range shown in the left panel of Fig. 3.32 comes mainly from the $5d$ states. The band broadening under pressure and the resulting decrease of the DOS can clearly be seen. It is obvious that the Fermi level lies in a flat valley of the DOS and this does not change under pressure. But the extrema in the band structure should give rise to anomalies in the DOS [5]. In the hope of finding them, the five panels

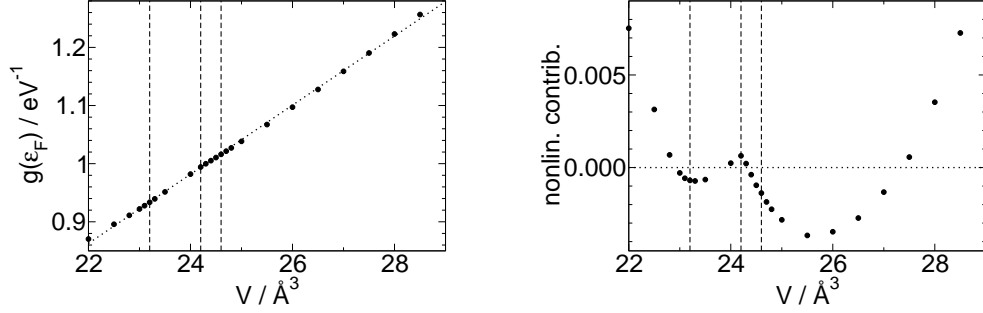


Figure 3.33: Left panel: DOS at the Fermi energy versus volume. The dotted line shows a linear function fitted to the data. The dashed lines mark those volumes, where the Lifshitz transitions take place. Right panel: Same as left panel but the slope of the fitted function has been subtracted from the data. The fact that these data differ in the fourth digit from those presented in Fig. 3.32 is due to different calculational schemes for $g(\varepsilon)$ and $g(\varepsilon_F)$ implemented in FPLO.

on the right of Figure 3.32 display an about hundredfold magnification of the DOS around the Fermi energy. Here a peak is seen, which crosses the Fermi level at that pressure, when the neck is created. The fact that the peak changes its shape at different volumes hints at a not sufficient \mathbf{k} -point resolution, though the DOS in this figure has been obtained with 96^3 \mathbf{k} -points. Despite the huge number of \mathbf{k} -points, structures smaller than 50 meV could not be unambiguously resolved.

A different view on the DOS is presented in Figure 3.33. Here, the DOS at the Fermi level is shown against volume (left panel). The locations of the Lifshitz transitions are denoted by dashed lines. It is remarkable, that the DOS at the Fermi level decreases almost linearly with decreasing volume. The dotted line is a linear function fitted to the data. Again, at the Lifshitz transitions nothing is seen. To enlarge possible non-linearities the slope of the fitted function has been subtracted from the data, shown in the right panel of Fig. 3.33. Small contributions from higher order terms as well as a peak are obvious. This peak is the same peak than the peak in Fig. 3.32, right panels. It is striking, that the maximum of the peak lies exactly at that energy, where the neck is created. It is also remarkable that there is no anomaly seen at that energy, where the ellipsoid at the Γ -point is formed. The energy, at which the ellipsoid at the L-point forms, lies in a minimum

of the DOS. Small differences between the data shown in Figures 3.32 and 3.33 are due to a different calculational scheme implemented in FPLO to calculate the DOS at the Fermi level.

To answer the question, why there is no anomaly in the DOS due to the Lifshitz transition at the Γ -point, $\delta g(\varepsilon)$ (see Eq. (2.78)) has been estimated. For this task the maximum at the Γ -point in the band structure (Figure 3.31) has been fitted by a parabola $f(k_i) = a_{i0} + a_{i1}k_i + a_{i2}k_i^2$ in all three directions of \mathbf{k} -space. Then the absolute value of the coefficient $|a_{i2}|$, which determines the curvature of the parabola was set equal to $\hbar^2/2m_i$ (compare Eq. (2.58)). This yields

$$\begin{aligned}\frac{\hbar^2}{2m_x} &= 171.4 \text{ eV}\text{\AA}^2 \\ \frac{\hbar^2}{2m_y} &= 161.4 \text{ eV}\text{\AA}^2 \\ \frac{\hbar^2}{2m_z} &= 97.1 \text{ eV}\text{\AA}^2\end{aligned}\tag{3.1}$$

It can be shown, that in a hexagonal environment $\hbar^2/2m_x = \hbar^2/2m_y$. The fact that in Eq. (3.1) $\hbar^2/2m_x$ and $\hbar^2/2m_y$ differ by 6% results from inaccuracies.

With $V = 27.87 \text{\AA}^3$ we can write

$$\delta g(\varepsilon) = -\frac{V}{\pi^2 \hbar^3} \sqrt{2m_x m_y m_z} \sqrt{\varepsilon_{cr} - \varepsilon} \tag{3.2}$$

$$= 4.43565 \text{\AA}^3 \sqrt{\frac{2m_x}{\hbar^2} \frac{2m_y}{\hbar^2} \frac{2m_z}{\hbar^2}} \sqrt{\varepsilon_{cr} - \varepsilon} \tag{3.3}$$

$$= \frac{4.43565 \text{\AA}^3 \sqrt{-0.0814 \text{ eV} - \varepsilon}}{\sqrt{171.4 \text{ eV}\text{\AA}^2 \cdot 161.4 \text{ eV}\text{\AA}^2 \cdot 97.1 \text{ eV}\text{\AA}^2}} \tag{3.4}$$

$$\approx 0.003 \text{ eV}^{-3/2} \sqrt{-0.0814 \text{ eV} - \varepsilon} \tag{3.5}$$

In a distance of about 0.0186 eV below the critical energy the contribution to the DOS due to this small ellipsoid amounts to $\delta g(-0.1) \approx -0.0004/\text{eV}$. This contribution is so small that it cannot be seen even on the enlarged scales in the right panels of Figures 3.32 and 3.33.

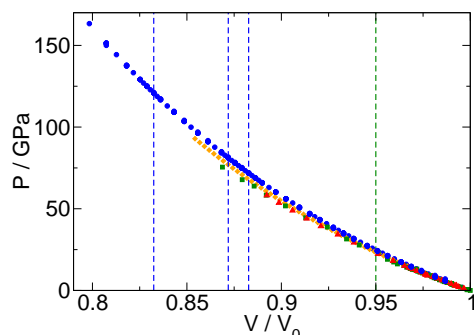


Figure 3.34: Equation of state of Osmium. The blue circles are our calculations. The green squares and the red triangles are experimental data taken from the publications of Occelli *et al.* [8] and Takemura [9] respectively. Yellow diamonds denote calculations done by Ma *et al.* [52]. The green dashed lines denotes the volume where Occelli *et al.* [8] claimed to find a Lifshitz transition. The blue dashed lines correspond to the volumes where we found Lifshitz transitions.

3.3.6 Lattice geometry under pressure

In this section the change of the unit cell volume and the c/a ratio under hydrostatic pressure are explored. As mentioned above, Occelli *et al.* [8] claimed to find a kink in $(c/a)(P)$ at a pressure of about 25 GPa, which was not seen by Takemura [9]. Ma *et al.* [52] did electronic structure calculations with the aim to find a reason for this kink but they did not find any reason.

In this work the pressure-volume dependence was calculated in two ways. On the one hand, different equations of state [32] were fitted to $E(V)$ (Fig. 3.25). On the other hand, since the fitting procedure will remove any anomaly, the derivative of $E(V)$ was calculated numerically by means of the three-point formula, $f'((x_1 + x_2)/2) \approx (f(x_2) - f(x_1))/(x_2 - x_1)$, considering neighboring V values. The resulting $P(V)$ is in perfect agreement with the $P(V)$ obtained by the fitting procedure: for 80% of the pressure range between zero and 180 GPa, our numerical derivative lies within the $P(V)$ values spanned by the different analytic fits. The maximum difference between any of the analytic fits and the numerical fit amounts to 0.2 GPa, and the mean difference amounts to 0.1 GPa.

Figure 3.34 shows the equation of state $P(V/V_0)$ of Osmium. The blue

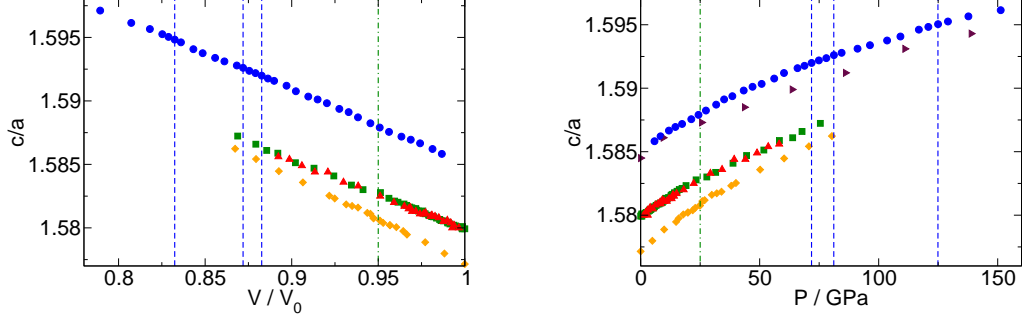


Figure 3.35: Left panel: relaxed c/a ratio against normalized volume. Right panel: relaxed c/a ratio against pressure. The meaning of the symbols is the same than in Fig. 3.34. Additional data from calculations by Sahu and Kleinman are denoted by violet triangles in the right panel [48]. Error-bars are below symbol size.

circles are our calculations. Green squares and red triangles are experimental data taken from the publications of Occelli *et al.* [8] and Takemura [9] respectively. Yellow diamonds denote calculations done by Ma *et al.* [52]. The green dashed line denotes the volume where Occelli *et al.* [8] claimed to find a Lifshitz transition. The blue dashed lines correspond to the volumes where we claim to have found Lifshitz transitions (compare Section 3.3.3). For low pressures calculations and experiments are in perfect agreement. At higher pressures there are small deviations.

In the left panel of Figure 3.35 the relaxed c/a ratio against normalized volume is plotted. Blue circles show our calculations done with FPLO. The green squares and the red triangles are experimental data taken from the publications of Occelli *et al.* [8] and Takemura [9] respectively. Yellow diamonds denote calculations done by Ma *et al.* [52]. In contradistinction to our calculations they used pseudopotentials instead of doing all-electron calculations and for the exchange-correlation potential they used GGA instead of LDA, what we used. Blue dashed lines denote those volumes/pressures, where we found Lifshitz transitions, the green dashed line denotes the volume/pressure, where Occelli *et al.* [8] claimed to find a Lifshitz transition. The experimental data are in perfect agreement, the c/a ratio Ma and Co-workers found, is a little bit too small and – what cannot be seen in this plot

	χ_n	σ	$V_0/\text{\AA}^3$	A	B
exp. (Occelli <i>et al.</i> [8])	0.73	$7.4 \cdot 10^{-5}$	27.949	$-0.0539(4)$	$1.6339(4)$
exp. (Takemura [9])	1.22	$1.2 \cdot 10^{-4}$	27.977	$-0.0540(6)$	$1.6339(6)$
this work		$5.9 \cdot 10^{-5}$	27.87	$-0.0594(2)$	$1.6445(1)$
calc. (Ma <i>et al.</i> [52])		$8.1 \cdot 10^{-5}$	28.48	$-0.0678(6)$	$1.6450(6)$

Table 3.1: Quality of linear fits to the $(c/a)(V/V_0)$ data displayed in Figure 3.35, left panel, in the range $0.87 < V/V_0 < 1$. For the definition of χ_n and σ see text. The fourth column displays the values used for V_0 . Values of adjustable parameters are given in the last two columns.

– their zero pressure volume is about 1.85% too large. FPLO yields a c/a ratio, which is about 0.005 too large but shows the same change with pressure than the measured data. It seems that the relaxed c/a ratio depends linearly on unit cell volume. No anomaly is seen neither where we found Lifshitz transitions nor at the location proposed by Occelli *et al.*.

Fitting a linear function $c/a = A \cdot (V/V_0) + B$ to each set of data and accounting for the known uncertainties of the experimental values yields the following standard deviation σ displayed in Table 3.1 for the volume-range $0.87 < V/V_0 < 1$. To characterize the quality of the fits, Table 3.1 displays also $\chi_n = \sqrt{\chi^2/(n - n_a)}$ where χ^2 denotes the sum of the error weighted square deviations, n the number of the data points, and n_a the number of adjustable parameters, here 2. These small deviations from a straight line support our opinion that $(c/a)(V/V_0)$ is well described by a linear function. From this finding we presume that there should be no kink in the c/a ratio versus pressure because Takemura stated in [53]: “*For the study of delicate changes in the axial ratios, it is better to plot the axial ratios as a function of the relative volume V/V_0 , where V_0 denotes the volume of each metal at atmospheric pressure [...]. This kind of plot is free from the uncertainty in pressure determination.*” Otherwise, if there would be a kink in $(c/a)(P)$ but not in $(c/a)(V/V_0)$ this would imply a kink in the equation of state $P(V)$, which is not the case as visible in Figure 3.34.

The right panel of Figure 3.35 shows the c/a ratio versus pressure, where Occelli and Co-workers [8], Ma and Co-workers [52] as well as Sahu and Kleinman [48] claim to find a kink at 25 GPa, 27 GPa, and 9.5 GPa, respectively. The symbols are the same as in the left panel. Calculations by Sahu and Kleinman [48] are denoted by violet triangles. They have done fully rela-

tivistic full-potential linearized augmented plane-wave calculations applying LDA. As mentioned above, to our opinion there is no kink in $(c/a)(P)$ because it is not a piecewise linear function but a non-linear smoothly curved function. This can be easily proved. There is no doubt that $(c/a)(V/V_0)$ is a linear function (compare Figure 3.35, left panel). If $(c/a)(P)$ is piecewise linear, then $P(V/V_0)$ would be piecewise linear as well. By looking at Figure 3.34 one can easily convince oneself that the equation of state is not piecewise linear, which is supported by the fact, that the pressure derivative of the bulk modulus B is non-zero (Occelli *et al.* [8] measured $B' \approx 4$ in Osmium), which implies that a Taylor expansion of $P(V/V_0)$ consists of at least second order terms.

In Ref. [8] Occelli *et al.* argued that dividing the measured pressure-range in two smaller ranges $0 < P < 25$ GPa and $25 \text{ GPa} < P$ and applying a piece-wise linear fit gives a much better fit than fitting the whole region with one linear function. For non-linear functions it is always the case, that a subdivision of the range of values to be fitted yields a much better linear fit, than a linear fit over the whole region would do. In the next section we will derive a smooth function, that fits the whole region at least as good as two linear pieces.

3.3.7 A good fit to $(c/a)(P)$

As mentioned in the previous section, we assume that $(c/a)(V/V_0)$ can be approximated by a linear function (compare Figure 3.35, left panel):

$$(c/a)(V/V_0) = \frac{c_0}{a_0} + d \cdot (V/V_0 - 1) , \quad a_0, c_0 > 0 \wedge d < 0 \quad (3.6)$$

For simplicity the equation of state will be approximated by a second order polynomial:

$$P(V/V_0) = p_2(V/V_0)^2 + p_1(V/V_0) - (p_1 + p_2) , \quad p_1 < 0 \wedge p_2 > 0 \quad (3.7)$$

Solving Eq. (3.6) for V/V_0 and substituting it in Eq. (3.7) yields

$$(c/a)(P) = (c/a)_m + \sqrt{\frac{d^2}{p_2}(P + P_m)} \quad (3.8)$$

with

$$(P_m, (c/a)_m) = \left(\frac{1}{p_2} \left(\frac{p_1}{2} + p_2 \right)^2, \frac{c_0}{a_0} - d - \frac{dp_1}{2p_2} \right). \quad (3.9)$$

	Eq. (3.8)		piece-wise linear function			
	χ_n	σ	kink: 25 GPa		kink: 27 GPa	
	χ_n	σ	χ_n	σ	χ_n	σ
exp. (Occelli <i>et al.</i> [8])	0.69	$6.8 \cdot 10^{-5}$	0.71	$7.4 \cdot 10^{-5}$	0.85	$8.5 \cdot 10^{-5}$
exp. (Takemura [9])	1.27	$1.3 \cdot 10^{-4}$	1.28	$1.3 \cdot 10^{-4}$	1.26	$1.3 \cdot 10^{-4}$
this work		$7.5 \cdot 10^{-5}$		$1.1 \cdot 10^{-4}$		$1.0 \cdot 10^{-4}$
calc. (Ma <i>et al.</i> [52])		$7.8 \cdot 10^{-5}$		$1.0 \cdot 10^{-4}$		$9.7 \cdot 10^{-5}$

Table 3.2: Quality of different fits to the data displayed in Figure 3.35, right panel, in the pressure range between zero and 60 GPa. For the definition of χ_n and σ see Section 3.3.6. Values of adjustable parameters are given at the end of this chapter.

Fitting $(c/a)(P)$ with Eq. (3.8) and comparing the standard deviation σ with σ of a piecewise linear fit, Table 3.2, one can see that the size of the standard deviation is the same, no matter if we fit the data with a piece-wise linear function or with the square root function of Eq. (3.8). The value range for P ($0 \leq P \leq 60$ GPa) was chosen such, that it is covered by all data sets. (We do not take into account the data by Sahu and Kleinman, since they have only four points in the considered pressure range.) To stay with three parameters we assumed the kink in the piece-wise linear fits to be fixed at the suggested 25 GPa (Occelli *et al.* [8]) and 27 GPa (Ma *et al.* [52]), respectively. Additionally for the data by Occelli *et al.*, we performed a four parameter piece-wise linear fit, allowing the critical pressure P_c to vary: Only a slightly better approximation was obtained ($\chi_n = 0.51$ for the complete data set), but P_c amounts to 19 ± 2 GPa.

To fit a smoothly curved function with four fitting parameters, for simplicity

$$(c/a)(P) = b_0 + b_1P + b_2P^2 + b_3P^3 \quad (3.10)$$

was chosen. For better comparison a three parameter fit was done with Eq. (3.10) as well by setting $b_3 = 0$. The results are displayed in Table 3.3. From these we conclude that $(c/a)(P)$ is equally well fitted by different smoothly curved non-linear functions with three parameters. Including a further parameter does not improve the fit.

	χ_n	σ	b_0	$10^4 b_1$	$10^7 b_2$	$10^9 b_3$
Occ. <i>et al.</i> [8]	0.69	$7.6 \cdot 10^{-5}$	1.579928(9)	1.32(2)	-5.9(6)	
Occ. <i>et al.</i> [8]	0.68	$6.9 \cdot 10^{-5}$	1.57993(1)	1.35(4)	-9(3)	4(4)
Tak. [9]	1.24	$1.24 \cdot 10^{-4}$	1.57991(4)	1.27(5)	-4.8(8)	
Tak. [9]	1.26	$1.26 \cdot 10^{-4}$	1.57993(6)	1.2(1)	-2(4)	-3(5)
this work		$5.7 \cdot 10^{-5}$	1.58513(6)	1.29(4)	-5.0(7)	
this work		$5.5 \cdot 10^{-5}$	1.58524(9)	1.1(1)	1(5)	-7(5)
Ma <i>et al.</i> [52]		$8.3 \cdot 10^{-5}$	1.57720(6)	1.68(5)	-8(1)	
Ma <i>et al.</i> [52]		$8.05 \cdot 10^{-5}$	1.57715(7)	1.8(1)	-16(5)	10(7)

Table 3.3: Quality of polynomial fits (parabolic and cubic, Eq. (3.10)) to the data displayed in Figure 3.35, right panel, in the pressure range between zero and 60 GPa. For the definition of χ_n and σ see Section 3.3.6. Values of adjustable parameters are given in columns 4 to 7.

3.3.8 Conclusions

We have calculated the total energy, Fermi surface, band structure and DOS of Osmium up to a pressure of about 180 GPa. Our electronic structure calculations yield a relative accuracy of c/a comparable with the relative accuracy of advanced diffraction methods.

The result of our study is, that Osmium shows three Lifshitz transitions at higher pressures than proposed. Their origin lies in three maxima of the band structure crossing the Fermi energy under pressure. The corresponding van Hove singularities in the DOS seem to be too small to be measurable.

To observe the Lifshitz transitions experimentally we suggest measurements of the resistivity of Osmium at low temperature under pressure because at least the transition, where the second sheet of Fermi surface opens in z -direction should be observable in a resistance measurement.

Furthermore, we could show, that an electronic origin for a possible kink in the c/a ratio versus pressure at about 25 GPa can be excluded. Moreover, our statistical analysis of the data exhibits that $(c/a)(P)$ can be equally well fitted by a smooth function and thus the data do not allow to draw any clear conclusion about a possible anomaly.

3.3.9 Values of adjustable parameters used in Table 3.2

Square-root fit to $(c/a)(P)$ (Eq. (3.8)):

	$(c/a)_m$	$\sqrt{d^2/p_2}/\text{GPa}^{-1/2}$	P_m/GPa
exp. (Occelli <i>et al.</i> [8])	1.572(1)	0.00146(9)	28(5)
exp. (Takemura [9])	1.572(2)	0.0015(1)	30(9)
this work	1.5753(8)	0.00162(5)	37(4)
calc. by Ma <i>et al.</i> [52]	1.5708(10)	0.00157(8)	16(4)

Piece-wise linear fit to $(c/a)(P)$, kink at 25 GPa:

A - c/a at $P = 0$ GPa

B - slope between 0 GPa and 25 GPa

C - slope between 25 GPa and 60 GPa

	A	$10^4 B/\text{GPa}^{-1}$	$10^4 C/\text{GPa}^{-1}$
exp. (Occelli <i>et al.</i> [8])	1.579933(9)	1.23(2)	0.80(3)
exp. (Takemura [9])	1.57995(4)	1.17(3)	0.86(3)
this work	1.58525(2)	1.117(8)	0.955(6)
calc. by Ma <i>et al.</i> [52]	1.57729(7)	1.46(3)	1.06(4)

Piece-wise linear fit to $(c/a)(P)$, kink at 27 GPa:

A - c/a at $P = 0$ GPa

B - slope between 0 GPa and 27 GPa

C - slope between 27 GPa and 60 GPa

	A	$10^4 B/\text{GPa}^{-1}$	$10^4 C/\text{GPa}^{-1}$
exp. (Occelli <i>et al.</i> [8])	1.579935(2)	1.219(14)	0.78(4)
exp. (Takemura [9])	1.57995(4)	1.16(3)	0.84(3)
this work	1.58525(2)	1.113(8)	0.940(7)
calc. by Ma <i>et al.</i> [52]	1.57730(6)	1.45(3)	1.02(4)

Chapter 4

SUMMARY

The aim of this thesis was to find Lifshitz transitions, which are topological changes of the Fermi surface. The materials under consideration had been YCo_5 and LaCo_5 as examples for magnetic compounds and the element Osmium as an example for a non-magnetic material. All these materials exhibit hexagonal symmetry.

In all cases the question arose, if the corresponding van Hove singularities are large enough to cause detectable anomalies in the elastic properties. Here, detectable means measurable by nowadays experimental techniques and computable within the accuracy reachable in nowadays computer calculations.

To shift the van Hove singularities through the Fermi energy we used hydrostatic pressure, which is mimicked in the computations by decreasing the volume of the unit cell, where the ratio of the unit cell dimensions c/a is adjusted such that $E_{total}(V) = \min_{(c/a)} E_{total}(V, c/a)$.

In the case of YCo_5 our calculations yield a first order Lifshitz transition. Here, an extraordinarily large peak in the spin-up part of the DOS, which is caused by a nearly dispersionless band in the hexagonal plane, crosses the Fermi level under a pressure of about 21 GPa. Thus, the spin-up $3d$ states

become partly depopulated, which results in a drop of the total magnetic moment of 35%. Therefore the transition can be regarded as a transition from strong to weak ferromagnetism [33]. Further, the transition results in a volume collapse of 1.4%. Though the volume collapse is isomorphic, it exhibits the following anisotropy: while the lattice constant in the hexagonal plane is almost smoothly contracting with increasing pressure, the lattice constant in c -direction collapses at the transition-pressure. This volume collapse has been verified in experiment [7].

Analogous calculations have been performed for the similar compound LaCo_5 . Here as well we predict a first order Lifshitz transition, taking place at a pressure of about 23 GPa. Again we find a volume collapse under pressure together with a decrease of the magnetic moment. The relative volume change amounts to 1.3%. Like in YCo_5 , the unit cell dimensions in the hexagonal plane are decreasing almost smoothly with pressure but in c -direction a jump occurs at the transition-pressure. Also the mechanism of the transition is the same than in YCo_5 .

It would be interesting to investigate the origin of the fact that the mentioned band is nearly dispersionless. Is it caused only by the symmetry of the unit cell? Maybe a tight binding model can clarify this question. Furthermore experiments measuring the magnetic moment of YCo_5 and LaCo_5 under pressure could provide a direct proof of the magneto-elastic origin of the volume collapse. For YCo_5 such experiments are planned [54]. In the case of LaCo_5 an experimental verification of our prediction concerning the isomorphic volume collapse would be interesting, too.

For Osmium we find, that LDA reproduces the ground state volume very well. Furthermore, we could detect three Lifshitz transitions taking place at very high pressures of about 72 GPa, 81 GPa, and 122 GPa. At first, a hole ellipsoid appears at the Γ -point ($V = 24.6 \text{ \AA}^3$, $P \approx 72 \text{ GPa}$), then a neck is created at the symmetry-line LH ($V = 24.2 \text{ \AA}^3$, $P \approx 81 \text{ GPa}$), and finally a hole ellipsoid appears at the L-point ($V = 23.2 \text{ \AA}^3$, $P \approx 122 \text{ GPa}$). Due to a degeneracy in the band structure, the hole ellipsoid at the L-point appears at the same pressure when the necks, situated at the symmetry-lines LH merge at L. The corresponding van Hove singularities in the DOS are very tiny and thus no anomalies in the elastic properties could be detected. We suggest to measure the transport properties of Osmium under pressure since such experiments are more sensitive to topological changes of the Fermi surface than the elastic properties.

Furthermore, we showed that the kink in c/a at 25 GPa and at 27 GPa

found by Ocelli *et al.* [8] and Ma *et al.* [52], respectively, is not statistically significant and that $(c/a)(P)$ can be fitted equally well by a smooth function as by piece-wise linear functions as proposed in these references.

BIBLIOGRAPHY

- [1] P. Hohenberg and W. Kohn, Phys. Rev. **136**, B 864 (1964).
- [2] W. Kohn and L. J. Sham, Phys. Rev. **140**, A 1133 (1965).
- [3] E. H. Lieb, Int. J. Quantum Chem. **24**, 243 (1983).
- [4] K. Koepnik and H. Eschrig, Phys. Rev. B **59**, 1743 (1999), <http://www.fplo.de>.
- [5] I. M. Lifshitz, Sov. Phys. JETP **11**, 1130 (1960).
- [6] Y. M. Blanter, M. I. Kaganov, A. V. Pantsulaya, and A. A. Varlamov, Phys. Rep. **245**, 159 (1994).
- [7] H. Rosner, D. Koudela, U. Schwarz, A. Handstein, M. Hanfland, I. Opahle, K. Koepnik, M. Kuz'min, K.-H. Müller, J. A. Mydosh, and M. Richter, Nature Physics **2**, 469 (2006).
- [8] F. Occelli, D. L. Farber, J. Badro, C. M. Aracne, D. M. Teter, M. Hanfland, B. Canny, and B. Couzinet, Phys. Rev. Lett. **93**, 095502 (2004).
- [9] T. Kenichi, Phys. Rev. B **70**, 012101 (2004).
- [10] H. Eschrig, M. Richter, and I. Opahle, in *Relativistic Electronic Structure Theory - Part II: Applications*, edited by P. Schwerdtfeger (Elsevier, Amsterdam, 2004), pp. 723–776.

- [11] P. Strange, *Relativistic Quantum Mechanics - with Applications in Condensed Matter and Atomic Physics* (Cambridge University Press, Cambridge, 1998).
- [12] H. Eschrig, *The Fundamentals of Density Functional Theory* (Edition am Gutenbergplatz, Leipzig, 2003).
- [13] M. Richter, in *Handbook of Magnetic Materials*, edited by K. H. J. Buschow (North-Holland, Amsterdam, 2001), Vol. 13, pp. 87 – 228.
- [14] E. d. Trémolet de Lacheisserie, *Magnetostriction - Theory and Applications of Magnetoelasticity* (CRC Press, London, 1993).
- [15] J. Kübler, *International Series of Monographs on Physics - Theory of Itinerant Electron Magnetism*, Vol. 106 (Oxford University Press, Oxford, 2000).
- [16] M. I. Kaganov and Y. V. Gribkova, *Fiz. Nizk. Temp.* **17**, 907 (1991).
- [17] A. A. Varlamov, V. S. Egorov, and A. V. Pantsulaya, *Adv. Phys.* **38**, 469 (1989).
- [18] N. W. Ashcroft and N. D. Mermin, *Solid State Physics* (Saunders College, Philadelphia, 1976).
- [19] H. Eschrig, *Proc. 4th Annual Int. Symp. on Electronic Structure of Metals and Alloys*, pp. 17–27 (1974).
- [20] K. H. J. Buschow, *Rep. Prog. Phys.* **40**, 1179 (1977).
- [21] K. H. J. Buschow, in *Ferromagnetic Materials : A Handbook on the Properties of Magnetically Ordered Substances*, edited by E. P. Wohlfarth (North-Holland, Amsterdam, 1980), Vol. 1, Chap. 4, pp. 297–414.
- [22] H. Yamada, K. Terao, F. Ishikawa, M. Yamaguchi, H. Mitamura, and T. Goto, *J. Phys.: Condens. Matter* **11**, 483 (1999).
- [23] A. Chatterjee, A. K. Singh, and A. Jayaraman, *Phys. Rev. B* **6**, 2285 (1972).
- [24] P. W. Bridgman, *Proc. Am. Acad. Arts Sci.* **62**, 207 (1927).

- [25] P. W. Bridgman, Proc. Am. Acad. Arts Sci. **76**, 55 (1948).
- [26] K. Haule, V. Oudovenko, S. Y. Savrasov, and G. Kotliar, Phys. Rev. Lett. **94**, 036401 (2005).
- [27] A. K. McMahan, K. Held, and R. T. Scalettar, Phys. Rev. B **67**, 075108 (2003).
- [28] P. Villars and L. D. Calvert, *Pearson's Handbook of Crystallographic Data for intermetallic Phases* (ASM international, Ohio, 1991).
- [29] L. Steinbeck, M. Richter, and H. Eschrig, Phys. Rev. B **63**, 184431 (2001).
- [30] J. P. Perdew and Y. Wang, Phys. Rev. B **45**, 13244 (1992).
- [31] K. Schwarz and P. Mohn, J. Phys. F **14**, L129 (1984).
- [32] J. K. Dewhurst, *EOS version 1.0, Program for fitting energy-volume data* (2002), <http://exciting.sourceforge.net>.
- [33] J. J. M. Franse and R. J. Radwanski, in *Handbook of Magnetic Materials*, edited by K. Buschow (North-Holland, Amsterdam, 1993), Vol. 7, Chap. 5, p. 307.
- [34] W. A. J. J. Velge and K. H. J. Buschow, J. Appl. Phys. **39**, 1717 (1968).
- [35] M. I. Bartashevich and T. Goto, J. Magn. Magn. Mater. **196 – 197**, 651 (1999).
- [36] B. K. Godwal, A. Jayaraman, S. Meenakshi, R. S. Rao, S. K. Sikka, and V. Vijayakumar, Phys. Rev. B **57**, 773 (1998).
- [37] A. B. Garg, A. K. Verma, V. Vijayakumar, R. S. Rao, and B. K. Godwal, Phys. Rev. B **72**, 024112 (2005).
- [38] G. V. Sin'ko and N. A. Smirnov, JETP Lett. **79**, 537 (2004).
- [39] B. K. Godwal, P. Modak, and R. S. Rao, Solid State Commun. **125**, 401 (2003).

- [40] D. L. Novikov, M. I. Katsnelson, A. V. Trefilov, A. J. Freeman, N. E. Christensen, A. Svane, and C. O. Rodriguez, Phys. Rev. B **59**, 4557 (1999).
- [41] V. V. Kechin, Phys. Rev. B **63**, 045119 (2001).
- [42] G. Steinle-Neumann, L. Stixrude, and R. E. Cohen, Phys. Rev. B **63**, 054103 (2001).
- [43] G. V. Sin'ko and N. A. Smirnov, J. Phys.: Condens. Matter **17**, 559 (2005).
- [44] T. Kenichi, Phys. Rev. B **60**, 6171 (1999).
- [45] T. Kenichi, Y. Hiroshi, F. Hiroshi, and K. Takumi, Phys. Rev. B **65**, 132107 (2002).
- [46] L. Fast, J. M. Wills, B. Johansson, and O. Eriksson, Phys. Rev. B **51**, 17431 (1995).
- [47] H. Cynn, J. E. Klepeis, C. S. Yoo, and D. A. Young, Phys. Rev. Lett. **88**, 135701 (2002).
- [48] B. R. Sahu and L. Kleinman, Phys. Rev. B **72**, 113106 (2005).
- [49] M. Hebbache and M. Zemzemi, Phys. Rev. B **70**, 224107 (2004).
- [50] G. N. Kamm and J. R. Anderson, Phys. Rev. B **2**, 2944 (1970).
- [51] V. I. Smelyansky, A. Y. Perlov, and V. N. Antonov, J. Phys.: Condens. Matter **2**, 9373 (1990).
- [52] Y. M. Ma, T. Cui, L. J. Zhang, Y. Xie, G. T. Zou, J. S. Tse, X. Gao, and D. D. Klug, Phys. Rev. B **72**, 174103 (2005).
- [53] T. Kenichi, Phys. Rev. B **56**, 5170 (1997).
- [54] H. Rosner, private communication.

Danksagung

Als erstes möchte ich Herrn Prof. Eschrig danken, denn er hat diese Doktorarbeit ermöglicht und in seinen interessanten Vorlesungen konnte ich einiges lernen. Auch dafür, daß ich 2004 mit nach Californien durfte, möchte ich mich herzlich bedanken.

Herrn Prof. Christensen und Herrn Prof. Grin danke ich für die Übernahme der Gutachten.

Manuel Richter möchte ich herzlich danken für die wissenschaftliche Betreuung und das Korrekturlesen dieser Arbeit, hilfreiche physikalische Erklärungen und Diskussionen, sowie dafür, daß er ein Ansprechpartner war für alle Fragen, die während meiner Zeit am IFW aufkamen.

Besonders bedanken möchte ich mich bei Ulrike Nitzsche. Sie half schnell und kompetent bei allen möglichen Computerproblemen und ich konnte von ihr die praktische Shell-Programmierung lernen.

Herrn Möbius danke ich für die Vorlesung in angewandter Numerik, in der ich nützliches Wissen für das Schreiben von Computerprogrammen erwerben konnte. Desweiteren möchte ich mich bei ihm für die schnelle und kompetente Hilfe bei numerischen Problemen und bei der Fehlerrechnung bedanken.

Ich möchte mich bei meinen Zimmerkollegen, insbesondere Ingo Opahle und Ferenc Tasnadi bedanken für die Hilfe bei allen Fragen, die im Arbeitsalltag so auftauchten.

Klaus Koepernik danke ich für Ratschläge beim Programmieren und bei mathematischen Problemen, sowie für die Überlassung von diversen Computerprogrammen.

Dank sei auch Helge Rosner für hilfreiche physikalische Erklärungen und Diskussionen, sowie für das Sport-Training, bei dem er mit Lob motivierte. So konnte ich entdecken, da ich gar nicht so unsportlich bin, wie ich immer dachte.

Bei Grit Rötzer und Angela Heinrich möchte ich mich für die Unterstützung beim Buchen von Dienstreisen und sonstigen administrativen Aufgaben bedanken.

Allen Mitarbeiterinnen und Mitarbeitern des ITF danke ich für die gute Arbeitsatmosphäre und Gespräche in Mittags- und Kaffeepausen. An dieser Stelle möchte ich meinen Dank auch allen Kolleginnen und Kollegen aussprechen, die durch das Kochen von Tee und das Mitbringen von leckerem Kuchen für das leibliche Wohl gesorgt haben.

Den Bibliothekarinnen Frau Schlenkrich und Frau Richter möchte ich für die Literaturbeschaffung danken.

Yanming Ma, Daniel L. Farber, Leonard Kleinman und B. R. Sahu danke ich für das Schicken von Daten. Dies ermöglichte es mir, meine Ergebnisse mit anderen detailliert zu vergleichen.

Dem SFB 463 danke ich für die Finanzierung der Arbeit.

Ferner möchte ich Thorsten Renk danken, der mir das ansprechende Layout für meine Doktorarbeit zur Verfügung stellte.

Ludwig Kornau danke ich für lange Gespräche, in denen ich viele hilfreiche Tipps für das praktische Leben bekam.

Mein großer Dank gilt der ESG. Dort habe ich ein Zuhause und viele Freunde und Freundinnen gefunden, eine wunderbare Gemeinschaft erlebt, interessante Vorträge gehört und die Möglichkeit gehabt, mich selbst auszuprobieren und Stärken zu entdecken.

Desweiteren möchte ich allen danken, die mir beim Leben Lernen geholfen haben.

PUBLIKATIONSLISTE

VERÖFFENTLICHUNGEN/PUBLICATIONS

1. **D. Koudela**, M. Richter, A. Möbius, K. Koepnik, H. Eschrig
Lifshitz transitions and elastic properties of Osmium under pressure
Phys. Rev. B **74**, 214103 (2006), cond-mat/0607329.
2. H. Rosner, **D. Koudela**, U. Schwarz, A. Handstein, M. Hanfland, I. Opahle, K. Koepnik, M. Kuz'min, K.-H. Müller, J. Mydosh, M. Richter
Magneto-elastic lattice collapse in YCo_5
Nature Physics **2**, 469 (2006).
3. **D. Koudela**, C. Volpe
Charmonium production in relativistic proton-nucleus collisions: What will we learn from the negative x_F region?
Phys. Rev. C **69**, 054904 (2004), hep-ph/0301186.
4. **D. Koudela**
Formationszeiteffekte in der Produktion von Charmonia in Proton-Kern Kollisionen
Diplomarbeit, <http://www.ub.uni-heidelberg.de/archiv/3043>.

EINGELADENE VORTRÄGE/INVITED TALKS

1. *Lifshitz-transitions in YCo_5 and Osmium*
Seminarvortrag im Nanoscience-Center Jyväskylä, Finnland
25.4.2006

SONSTIGE VORTRÄGE/CONTRIBUTED TALKS

1. *Kollisionen von schweren Ionen, Quark-Gluon Plasma und J/ψ*
Vortrag im Doktorandinnen-Diplomandinnen-Interessierte-Treffen,
Universität Heidelberg
18.1.2002

2. *Formation time effects in charmonium production in pA-collisions*
Vortrag in einem Meeting zum HERA-B Experiment,
Max-Planck-Institut für Kernphysik, Heidelberg
15.3.2002
3. *Formation time effects in charmonium production in pA-collisions*
Vortrag auf dem internationalen Workshop „Charm Production: from
Threshold via SPS to RHIC and LHC“, ECT*, Trento, Italien
18.6.2002
4. *Formation time effects in charmonium production in pA-collisions*
Seminarvortrag in der Arbeitsgruppe „Nuclear physics“,
Institut für Theoretische Physik, Heidelberg
11.11.2002
5. *YCo_5 under pressure*
Seminarvortrag in der Abteilung „Theoretische Festkörperphysik“,
Leibniz-Institut für Festkörper- und Werkstoffforschung, Dresden
15.7.2003
6. *Zeigt YCo_5 ungewöhnliche Eigenschaften unter Druck?*
Fachvortrag auf der Deutschen Physikerinnentagung 2003, Augsburg
8.11.2003
7. *Magnetic and elastic properties of YCo_5 under pressure*
Vortrag auf der Winterschule des Leibniz-Institutes für
Festkörper- und Werkstoffforschung, Oberwiesenthal
16.1.2004
8. *Magnetic and elastic properties of YCo_5 under pressure*
Vortrag auf der Frühjahrstagung der
Deutschen Physikalischen Gesellschaft, Regensburg
8.3.2004
9. *Magnetic and elastic properties of YCo_5 under pressure*
Vortrag auf dem Workshop „Hands-on-FPLO“, UC Davis, Californien
19.6.2004
10. *Magnetic and elastic properties of YCo_5 under pressure*
Vortrag auf der Konferenz JEMS, Dresden
8.9.2004

11. *The Self-Interaction Correction (SIC)*
Vortrag auf dem Workshop „Hands-on-FPLO“, Dresden
30.3.2005
12. *Does Osmium show a Lifshitz transition under pressure?*
Vortrag auf der Konferenz ψ_k 2005, Schwäbisch Gmünd
20.9.2005
13. *Lifschitzübergänge in Osmium*
Fachvortrag auf der Deutschen Physikerinnentagung 2005, Darmstadt
28.10.2005
14. *Lifshitz-transitions in Osmium under pressure*
Seminarvortrag im ITF,
Leibniz-Institut für Festkörper- und Werkstoffforschung, Dresden
8.11.2005
15. *Lifshitz-transitions in Osmium under pressure*
Vortrag auf der Frühjahrstagung der
Deutschen Physikalischen Gesellschaft, Dresden
29.3.2006
16. *Lifshitz-transitions in Osmium*
Vortrag auf dem Workshop „Hands-on-FPLO“, Dresden
23.5.2006

POSTER/POSTERS

1. *YCo₅ under pressure*
Post-deadline Poster auf der International Conference on Magnetism
Rom, Italien
27.7. – 1.8.2003

Versicherung

Hiermit versichere ich, dass ich die vorliegende Arbeit ohne unzulässige Hilfe Dritter und ohne Benutzung anderer als der angegebenen Hilfsmittel angefertigt habe; die aus fremden Quellen direkt oder indirekt übernommenen Gedanken sind als solche kenntlich gemacht.

Die Arbeit wurde bisher weder im Inland noch im Ausland in gleicher oder ähnlicher Form einer anderen Prüfungsbehörde vorgelegt.

Die vorliegende Arbeit wurde am Leibniz-Institut für Festkörper- und Werkstoffforschung Dresden unter der wissenschaftlichen Betreuung von Herrn Prof. Dr. H. Eschrig angefertigt.

Ich erkenne die Promotionsordnung der Fakultät für Mathematik und Naturwissenschaften der Technischen Universität Dresden an.

Dresden, den

.....
(Daniela Koudela)